The superficial tufted and mitral cell output neurons of the mouse olfactory bulb have dual roles in insulin sensing

Running Title: Insulin sensing superficial tufted cells

Louis John Kolling[3], Saptarsi Mitra[1,2], Catherine Anne Marcinkiewcz[2] and *Debra Ann Fadool[1,2, 3]

*Corresponding Author
319 Stadium Drive, Suite 3008
King Life Sciences Building
[1]Department of Biological Science
[2]Program in Neuroscience and [3]Institute of Molecular Biophysics
The Florida State University
Tallahassee, FL 32306
USA
dfadool@bio.fsu.edu
850 644-4775

[2]Department of Neuroscience & Pharmacology
The University of Iowa
Iowa City, IA 52242 USA

Number of pages = 40
Number of figures = 8
Number of tables = 2
Supplementary statistical table (excel) = 1

Number of words in manuscript excluding abstract, methods and citations = 6695

KEY WORDS = Kv1.3 channel, insulin, olfactory bulb, tufted cells, output neurons, olfaction

SUMMARY STATEMENT

Superficial tufted cells, as output neurons of the olfactory bulb, were electrophysiologically studied to be insulin sensitive. Brain insulin signaling represents a manner in which olfactory and metabolic circuitry are intertwined.

ABSTRACT

The olfactory bulb (OB) contains multiple, parallel projection neurons to relay the nature of a stimulus. In a mouse *ex vivo* slice preparation, we used patch-clamp electrophysiology to measure intrinsic properties, excitability, action potential (AP) shape, voltage-activated conductances, and neuromodulation in the newly-categorized superficial tufted cells (sTCs) compared with those of mitral cells (MCs). We propose that a marked difference in voltage-dependent current represents distinct ion channel populations that affect the kinetics of action potentials, and evokes an increase in sTC firing frequency, albeit both types of projection neurons having similar AP spiking activity. Triple-colored immunofluorescence and RNA scope were used to detect co-localization of the Kv1.3 ion channel and the insulin receptor in sTCs, with ~73% of sTCs expressing both. The sTCs were modulated by bath application of insulin – increasing AP firing frequency by 97%, attributable to an 8% decrease in the intraburst interval, and a reduction of the latency to first spike by 37%. We conclude that there may be a range of neuromodulators of sTCs that may alter excitability and fine-tune olfactory information processing or metabolic balance.

INTRODUCTION

Sensory systems typically carry multiple types of parallel output, or projection neurons, to relay differing specificity with regards to the nature of the stimulus. The olfactory bulb (OB) processes electrically-encoded odor information, and relays it to overlapping, but not identical, cortical regions via two types of primary projection neurons – namely mitral (MCs) and tufted cells (TCs) (Price and Powell, 1970; Vaaga and Westbrook, 2016). Albeit both receiving synaptic connections from the olfactory sensory neurons (OSNs) at defined and evolutionarily-conserved integration units called glomeruli, less has been studied concerning TCs in terms of biophysical properties and sources of modulation (Liu and Shipley, 2008; Burton and Urban, 2014; Jones et al., 2020). We and other investigators typically recorded from both populations of neurons, referring to them collectively as M/TCs (Fadool and Levitan, 1998; Tucker and Fadool, 2002; Youngstrom and Strowbridge, 2015; Liu et al., 2016). In model organisms, such as drosophila and zebrafish, MCs and TCs are not readily distinguishable from one another (Nagayama et al., 2014). The neurolaminae of mice are significantly more distinct, allowing the complexity of the olfactory circuity to be more easily assessed.

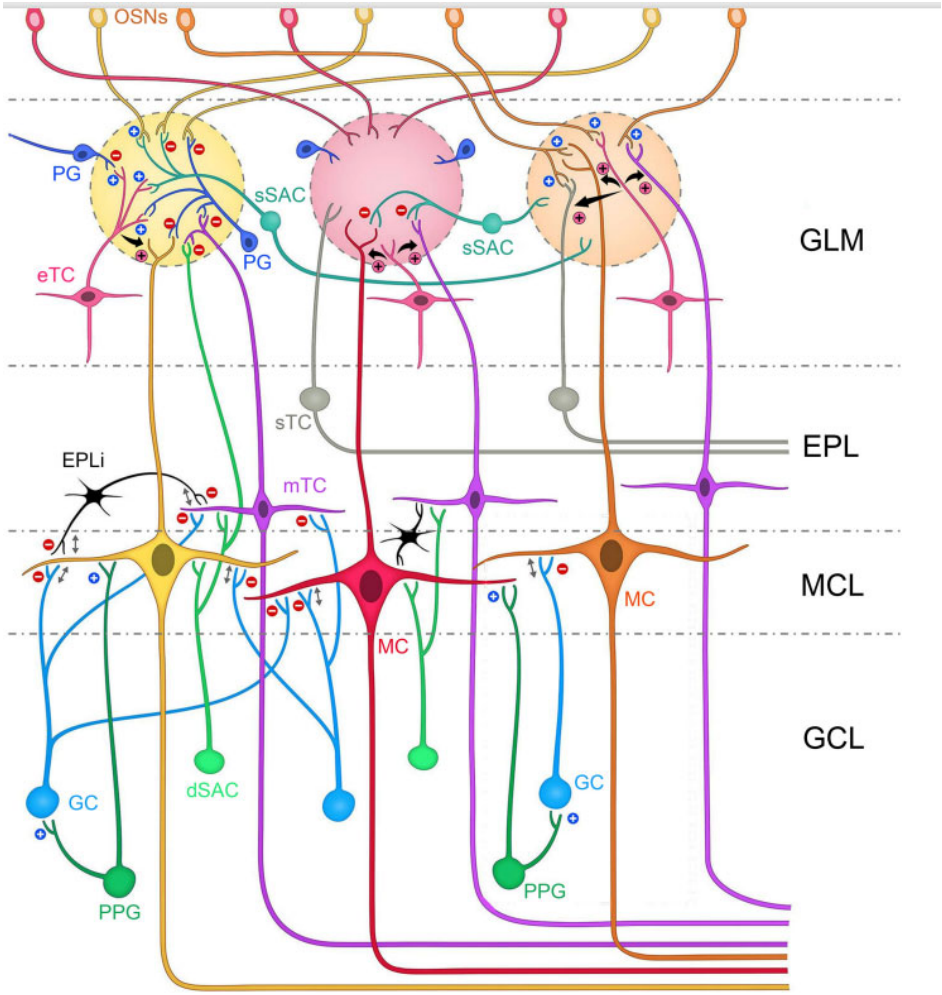

90 **Fig. 1**. **Categorization and interactions of the principal projection neurons of the olfactory**
91 **bulb.** The olfactory bulb neurolamina is divided across the glomerular layer (GLM), external
92 plexiform layer (EPL), the mitral cell layer (MCL), and the innermost granule cell layer (GCL). Also
93 shown is the olfactory mucosa containing the olfactory sensory neurons (OSNs). This schematic
94 highlights the four classes of output or projection neurons, namely the external tufted cells (eTCs,
95 pink), the superficial tufted cells (sTCs, gray), the middle tufted cells (mTCs, purple), and the mitral
96 cells (MCs, red). The soma of the eTCs are found within the GLM. The sTC soma reside in the
97 superficial one-third of the EPL. The deep two-thirds of the EPL contain both the mTCs and
98 misplaced MCs. The MCL houses the eponymous MCs. Blue plus signs (+) represent excitatory
99 synapses, red minus signs (-) represent inhibitory synapses, and pink plus signs (+) represent
100 excitatory dendro-dendritic interactions originating from external tufted cells (eTCs). Reciprocal
101 synapses are denoted by a double arrow. PG = periglomerular cell, sSAC = superficial short axon
102 cell, EPLi = interneuron of the external plexiform layer, GCL = granule cell layer, GC = granule cell,
103 PPG = preproglucagon neuron, dSAC = deep short axon cell. *Modified from Huang* et al. *2021.*

104

105

106

107 Like many budding areas of research, the standardization of categorical terminology is not
108 considered until there is enough information to classify. Jones et al. 2020 aptly stated that the
109 *"nomenclature around TC subtypes has been somewhat confusing in the field* (Jones et al.,
110 2020)." Both early works and more recent reviews describe 4 distinct classes of projection
111 neurons – external TC, internal TC, middle TC, and MC (Pinching and Powell, 1971a,b;
112 Mori, 1987; Shepherd, 2004; Hayar et al., 2004; Mori and Sakano, 2022). A more recent
113 work proposed to alternatively reclassify output neurons based upon size and location into
114 three types: putative MCs (pMC; >20 um diameter and located in the MCL), EPL located TC
115 (lower EPL TC; <20 um diameter), and putative TC (pTC; <20 um diameter located in the
116 MCL) (Gadiwalla et al., 2025). Herein, our study uses the naming convention originating
117 from Cajal and then reestablished by Jones et al. (2020), based upon the position of the TC
118 soma within its respective neurolamina – namely, external tufted cells (eTCs), middle tufted
119 cells (mTCs), and superficial tufted cells (sTCs) (**Fig. 1**). Of the three subclasses of TCs, the
120 eTC are the best studied. The eTCs are a select population of juxtaglomerular cells that
121 demonstrate rhythmic and spontaneous action potential bursting (Hayar et al., 2004a,b, 2005;
122 Antal et al., 2006; Zhou et al., 2006; Ma and Lowe, 2007; Liu and Shipley, 2008). The eTC
123 are known to receive monosynaptic input from olfactory sensory neurons (OSNs) and
124 establish glutaminergic synaptic connections to short-axon cells and periglomerular cells
125 within the bulb (Hayar et al., 2004a,b, 2005), and their activation can provide feedforward
126 excitation of MC (De Saint Jan et al. 2009). eTCs actually process sensory input before it
127 reaches the sTCs and MCs (De Saint Jan et al., 2009; Najac et al., 2011; Gire et al., 2012;
128 Igarashi et al., 2012; Vaaga and Westbrook, 2016). The eTCs receive the greatest signal from
129 activated OSNs, and stimulate neighboring sTCs, mTCs, and MCs via glutamatergic dendro-
130 dendritic interactions (De Saint Jan *et al*., 2009; Najac *et al*., 2011; Jones *et al*., 2020). This
131 feed-forward excitation from eTCs provides "biphasic input" to other M/TCs that may also
132 receive direct monosynaptic input from a specific OSN family member (Najac *et al*., 2011;
133 Vaaga and Westbrook, 2016; Jones *et al*., 2020).
134
135 Because the eTC are well characterized, and the mTCs are less accessible for patch-
136 clamp recordings, we decided to focus our study on a lesser known type of TC, the sTC,
137 which are expressed superficially in the external plexiform layer (EPL)(Jones et al., 2020;

138 Chen et al., 2024). mTC soma are found between the MCL and the inner (deep) two-thirds of
139 the external plexiform layer (EPL), whereas the soma of superficial tufted cells (sTCs) are
140 located in the outer (superficial) one-third of the EPL. Like MCs, sTCs and mTCs receive
141 input from olfactory sensory neurons (OSNs) at defined glomeruli, and pass sensory
142 information to various subcortical areas. The sTCs and mTCs, however, project, to distinctly
143 different brain regions than MCs; even if a M/TC pair projects to the same subcortical region,
144 it will project to different parts of it (Nagayama et al., 2010, 2014; Igarashi et al., 2012).
145 Excellent foundational work has been done to characterize the innate biophysical differences
146 between TCs and MCs (Burton and Urban, 2014), but the categorization of the assessed cells
147 preceded the boundaries set by the current naming methods (Jones et al., 2020). As such, no
148 previous report has characterized the innate biophysical differences between MCs and sTCs,
149 nor investigated the function of sTCs to sense metabolically-relevant molecules or
150 neuromodulators.
151
152 In this study, we compare the biophysical properties of MCs and sTCs in *ex vivo* brain slices
153 from male and female mice. Using current- and voltage-clamp recordings, we found that
154 action potential (AP) properties and voltage-activated currents differed between sTCs and
155 MCs. To better understand the complementary function of sTCs to MCs, we examined the
156 response of sTCs to a known modulator and a vestibule blocker of Kv1.3 – a predominant ion
157 channel carrying 60-80% of the outward current in MCs (Fadool and Levitan, 1998; Colley et
158 al., 2004). Our results directly show that sTCs are more excitable than MCs. This is correlated
159 with differing voltage-activated currents, and a differing AP shape. We further find that sTCs
160 are modulated by the presence of insulin, suggesting a role for sTCs in metabolic circuitry
161 (Fadool et al., 2004; Palouzier-Paulignan et al., 2012; Aimé et al., 2014). While both MC and
162 sTCs carry the role of propagating odor-coding information to higher cortical regions, they
163 have another role, hence a dual role, to encode metabolic state when insulin is present, either
164 locally or as modulated following food ingestion. The major olfactory output neurons hence
165 have a dual role – one for odor encoding, and a second for changed activity with metabolism.
166 Our study demonstrates that one downstream target, the Kv1.3 ion channel, is necessary for
167 the insulin-sensing property of sTCs, as it is in MCs (Fadool et al., 2004, 2011; Tucker et al.,
168 2013).

169
170
171
172 # RESULTS

173 **Superficial tufted cells have greater input resistance and slightly lower voltage-**
174 **activated current at hyperpolarizing potentials than that of mitral cells**

175 Superficial tufted cells (sTCs) have greater EPSC amplitude when stimulated by direct
176 olfactory sensory neuron activation over that of mitral cells (MCs) (Jones et al., 2020), albeit
177 both being the predominant output neurons of the OB. Less has been studied to reveal the
178 nature of intrinsic properties and voltage-activated conductances in sTCs. We used ex vivo
179 slice electrophysiology in the voltage-clamp configuration, therefore, to study intrinsic
180 properties as well as outward currents, which are largely driven by the Kv1.3 channel in MCs
181 (Fadool *et al*., 1997; Fadool and Levitan, 1998). The resting membrane potential (RMP) was
182 not significantly different between MCs and sTCs (MCs = -55.8 $\pm$ 6.3 mV (20) vs. sTCs = -
183 58.0 $\pm$ 6.5 mV (22); Student's *t*-test, p = 0.2906).
184
185 Macroscopic currents were acquired in response to a series of 400 ms duration (P_d) voltage
186 steps that increased in increments of 20 mV from -100 mV to +40 mV. The resulting current-
187 voltage (IV) relationship was plotted in **Fig. 2A** using the peak transient current value for each
188 step normalized to the +40 mV step. It was noted that the amplitude of the outward current at
189 hyperpolarizing potentials (a window between -60 to -20 mV) was significantly greater in
190 MCs vs. that of sTCs (**Fig. 2B**). A two-way repeated measure, mixed factor analysis of
191 variance (2-w RM mixed ANOVA) was applied using cell type and voltage as factors. There
192 was a main effect of cell type (F (1, 22) = 9.430; p = **0.0056) as well as a voltage x cell type
193 interaction (F (7, 154) = 5.542; p <0.0001). A Sidak's post-hoc test showed that the evoked
194 current was significantly greater for MCs at the -60 mV (p = 0.0202), -40 mV (p = 0.0049)
195 and -20 mV (p = 0.0311) voltage steps. This difference only existed in this hyperpolarized
196 window and was not observed once highly depolarized at the +40 mV step (**Fig. 2C**, MCs =
197 5180 $\pm$ 2540 pA (11) vs. sTCs = 3746 $\pm$ 1030 pA (13), Mann-Whitney U, p = 0.2066). We
198 next measured the kinetics of inactivation and deactivation for the voltage-activated currents
199 at a hyperpolarized (V_c = -40 mV) and depolarized (V_c = +40 mV) range, respectively. The

kinetics of inactivation (τ_{Inact}) did not differ between cell types (**Fig. 2D, Left**, MCs = 71.2 $\pm$ 19.0 ms (10) vs. sTCs = 57.0 $\pm$ 28.6 ms (13), Student's *t*-test, $p = 0.1894$) at V_c = -40 mV, however the kinetics of deactivation (τ_{Deact}) was significantly faster for sTCs at this command voltage (**Fig. 2D, Right**, MCs = 2.19 $\pm$ 0.67 ms (11) vs. sTCs = 1.47 $\pm$ 0.61 ms (13), Mann-Whitney U, $*p = 0.0107$). Neither time constant differed between cell types at a V_c = +40 mV step (**Fig. 2E**, τ_{Inact}: MCs = 75.6 $\pm$ 30.9 ms (11) vs. sTCs = 158 $\pm$ 140 ms (13), Mann-Whitney U, $p = 0.3031$; τ_{Deact}: MCs = 1.14 $\pm$ 0.41 ms (10) vs. sTCs = 1.12 $\pm$ 0.52 ms (13), Student's *t*-test, $p = 0.9043$). Overall, although sTCs tend to have higher input resistance than MCs, the outward voltage-activated currents of sTCs are less responsive to changes in voltage.

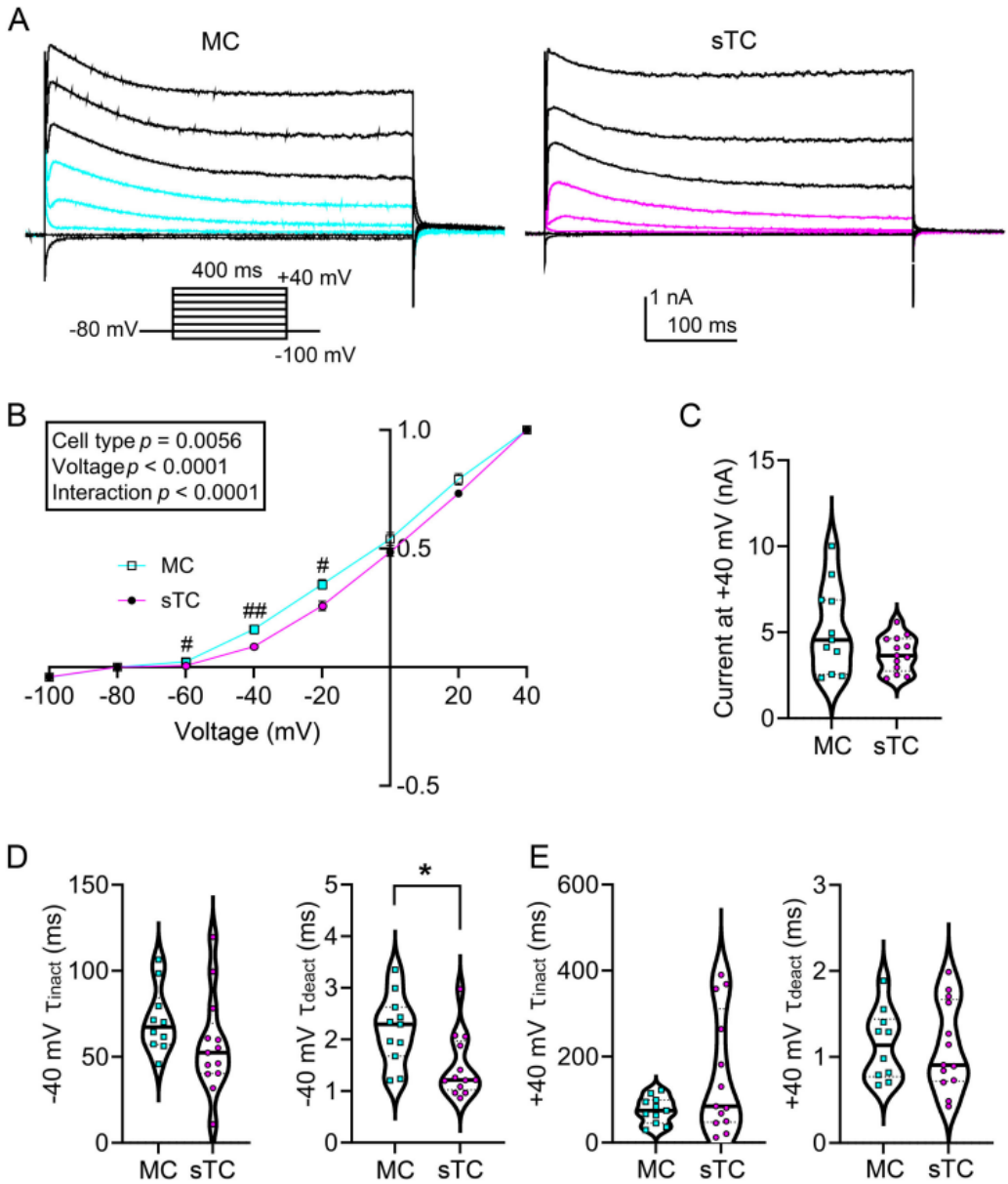

Fig. 2. Outward voltage-activated current properties of mitral cells and superficial tufted cells. ***A,*** Family of voltage-activated currents, V_h = -80 mV where V_c was stepped in 20 mV increments from -100 mV to +40 mV using a P_d = 400 ms. Colored sweeps correspond to significantly different colored data points in (***B***). ***B,*** Normalized IV plots (2-w mixed RM ANOVA, cell type ***p = 0.0056, Sidak's post-hoc test, $^{\#}p < 0.05$, $^{\#\#}p < 0.01$; voltage x cell type interaction ****$p < 0.0001$). ***C,*** Violin plot of non-normalized peak transient voltage-activated current at +40 mV, Mann-Whitney U. Violin plot of the *Tau* of inactivation (*left*) and deactivation (*right*) at **(D)** Vc = -40 mV and **(E)** +40 mV, respectively, Mann-Whitney U (*p = 0.0107). MC = mitral cell population sampled, sTC = superficial tufted cell population sampled.

241 **Kv1.2 and Kv1.3 expression is similar between superficial tufted and mitral**
242 **cells**

243 The drug MgTx is a selective blocker of Kv1.2 and Kv1.3 ion channels when applied to the
244 extracellular membrane at 1 nM concentration (Garcia-Calvo et al., 1993; Garcia et al., 1997;
245 Bartok et al., 2014). It has a slow k_{on} of 10 min and an even slower k_{off} of 2 h (Garcia-Calvo et
246 al., 1993; Nikouee et al., 2012; Chen and Chung, 2014), therefore, we did not attempt a
247 washout of the vestibule blocker during our patch recording. After collecting baseline voltage-
248 clamp recordings on MCs for 15 min, 1 nM MgTx was added to the bath to wash over the
249 slice for 15 min. Another set of voltage-clamp recordings was then collected (**Fig. 3A**). The
250 same repeated-measure paradigm was then applied to a separate group of sTCs (**Fig. 3B**).
251 MgTx reduced voltage-activated currents in both MCs and sTCs in a voltage-dependent
252 manner (**Fig. 3C).** Here, a 2-w mixed RM ANOVA was applied using drug and voltage as
253 factors. For the MC recordings, there was a main effect of drug ($F(1, 9) = 43.62$, ****$p <$
254 0.0001) as well as a voltage x drug interaction ($F(7, 63) = 43.86$, ****$p < 0.0001$). A Sidak's
255 post-hoc test demonstrated significant differences at the -20 mv ($^{\#\#\#}p = 0.0008$) voltage step
256 and all further depolarizing steps ($^{\#\#\#\#}p < 0.0001$). For the sTC recordings, there was a main
257 effect of drug ($F(1, 12) = 25.51$, ***$p = 0.0003$) as well as a voltage x drug interaction ($F(7,$
258 $60) = 19.87$, ****$p < 0.0001$). A Sidak's post-hoc test demonstrated significant differences at
259 -30 mv and above ($^{\#\#\#\#}p < 0.0001$). Using a 3-way mixed-effects analysis (3-w mixed RM
260 ANOVA), we found no difference in MgTx-mediated effects on voltage dependence between
261 MCs and sTCs (**Fig. 3C, Bottom**, voltage x cell type x drug interaction $F(7, 123) = 0.7633$, p
262 $= 0.6190$).
263
264
265
266
267
268
269
270
271

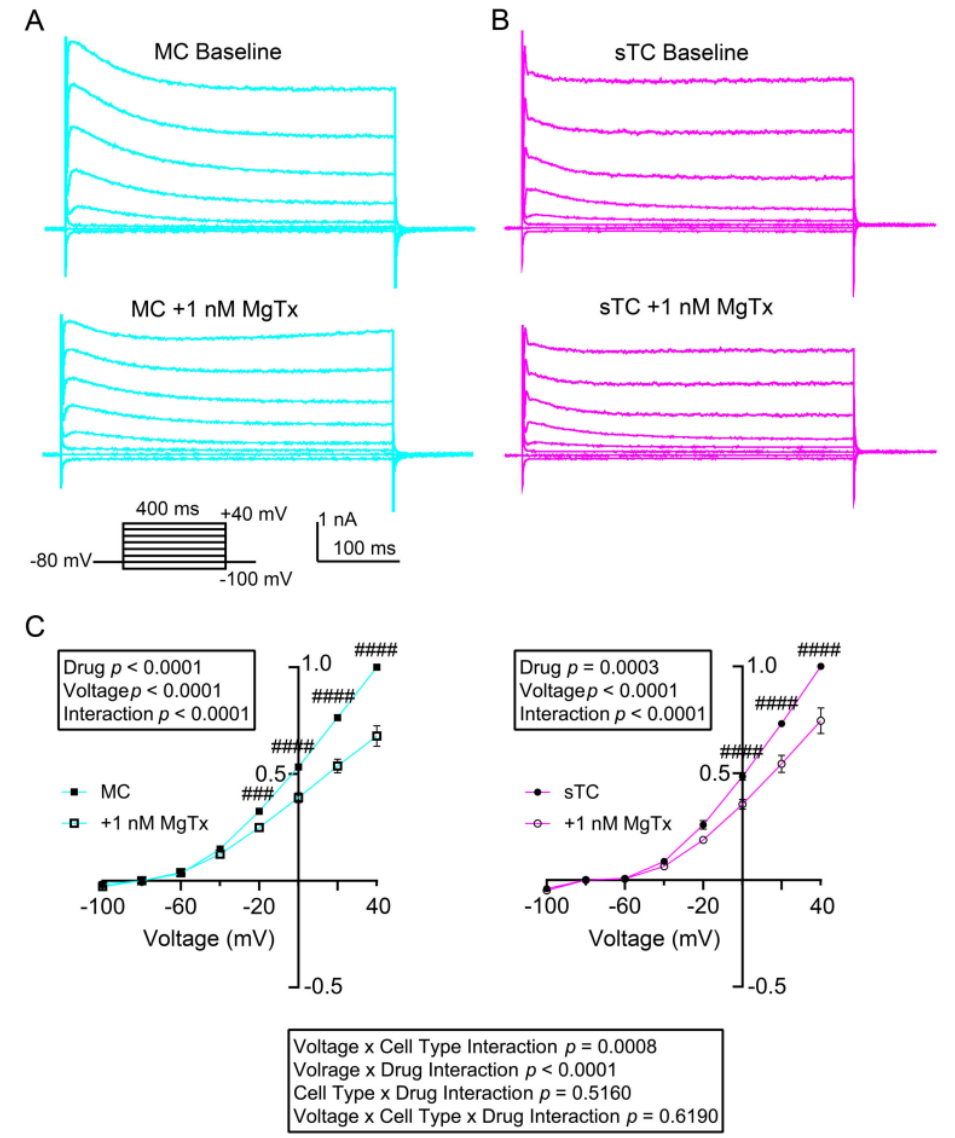

Fig. 3. Sensitivity of mitral and superficial tufted cells to a selective blocker of Kv channels. ***A,*** Family of voltage-activated currents recorded as in Figure 3 prior (***Top***, Baseline) and following (***Bottom***, +1 nM MgTx) 15-min bath application of margatoxin (MgTx) in a representative ***A,*** mitral cell (MC) and ***B,*** superficial tufted cell (sTC). ***C,*** Normalized IV plots prior (solid symbols) and following (open symbols) bath application of MgTx in a population of MCs (***Left,*** 2-w mixed RM ANOVA, drug F (1, 9) = 43.62, ****$p < 0.0001$, with a Sidak's post hoc test, $^{\#\#\#}p = 0.0008$, $^{\#\#\#\#}p < 0.0001$; voltage x drug interaction F (7, 63) = 43.86, ****$p < 0.0001$) and a population of sTCs (***Right,*** 2-w mixed RM ANOVA, drug ***$p = 0.0003$, Sidak's post-hoc test, $^{\#\#\#\#}p < 0.0001$; voltage x drug interaction ****$p < 0.0001$). ***C, Bottom*** – 3-way mixed RM ANOVA result comparing the two IV plots in ***C, Left-Right*** (3-w mixed RM ANOVA, voltage x cell type interaction F (7, 123) = 3.879, ***$p = 0.0008$; voltage x drug interaction F (7, 123) = 57.42, ****$p < 0.0001$; cell type x drug interaction F (1, 123) = 0.4244, $p = 0.5160$; voltage x cell type x drug interaction F (7, 123) = 0.7633, $p = 0.6190$).

286 **Superficial tufted cells are more excitable than mitral cells**

287 We next wanted to compare evoked AP firing frequency between MCs and sTCs as a metric
288 for cellular excitability. After obtaining the whole-cell configuration, cells were current-
289 clamped using a V_h of -60 mV (near RMP) for comparison of excitability across cell types.
290 Each MC or sTC was stimulated with a family of injected current steps that increased in 25
291 pA increments from -50 pA to 175 pA (**Fig. 4A**) to determine the threshold for first firing. On
292 average, the current needed to evoke APs (rheobase) was lower in sTCs than in MCs (**Fig. 4B**,
293 MCs = 69.3 $\pm$ 44.9 pA (22) vs. sTCs = 34.2 $\pm$ 24.1 pA (30), Mann-Whitney U, $^{**}p = 0.0021$).
294 Both cell types increased AP firing frequency in response to current step, but sTCs had a
295 significantly greater frequency than that of MCs (**Fig. 4C**). Here, we applied a 2-w mixed RM
296 ANOVA using cell type and current as factors. As anticipated, there was a main effect for
297 injected current ($F(7, 263) = 71.39$, $^{****}p < 0.0001$). There was also a main effect for cell
298 type ($F(1, 51) = 11.92$, $^{**}p = 0.0011$) and a current x cell type interaction ($F(7, 263) = 3.656$,
299 $^{***}p = 0.0009$). A Sidak's post-hoc test indicated a significant difference in current
300 dependence at the current injection window between 25 and 75 pA (25 pA - $^{\$\$}p = 0.0077$, 50
301 pA - $^{\$\$}p = 0.0017$, and 75 pA - $^{\$\$\$}p = 0.0001$). The increased AP firing frequency in response
302 to injected current was likely attributed to a change in interspike interval (ISI). As shown in
303 **Fig. 4D**, the ISI was shorter in sTCs compared to that of MCs. A 2-w mixed RM ANOVA
304 using cell type and injected current as factors demonstrated a main (negative) effect for
305 injected current ($F(1.643, 38.07) = 33.74$). There was also a main effect for cell type ($F(1,$
306 $49) = 37.53$, $^{****}p < 0.0001$) and a current x cell type interaction ($F(6, 139) = 5.873$, $^{****}p$
307 < 0.0001). A Sidak's post-hoc test indicated a significant difference between cell types at the
308 current injection window between 100 and 150 pA (100 pA - $^{\#}p = 0.0101$, 125 pA - $^{\#\#}p$
309 $= 0.0022$, and 150 pA - $^{\#}p = 0.0294$).
310
311
312
313
314
315
316

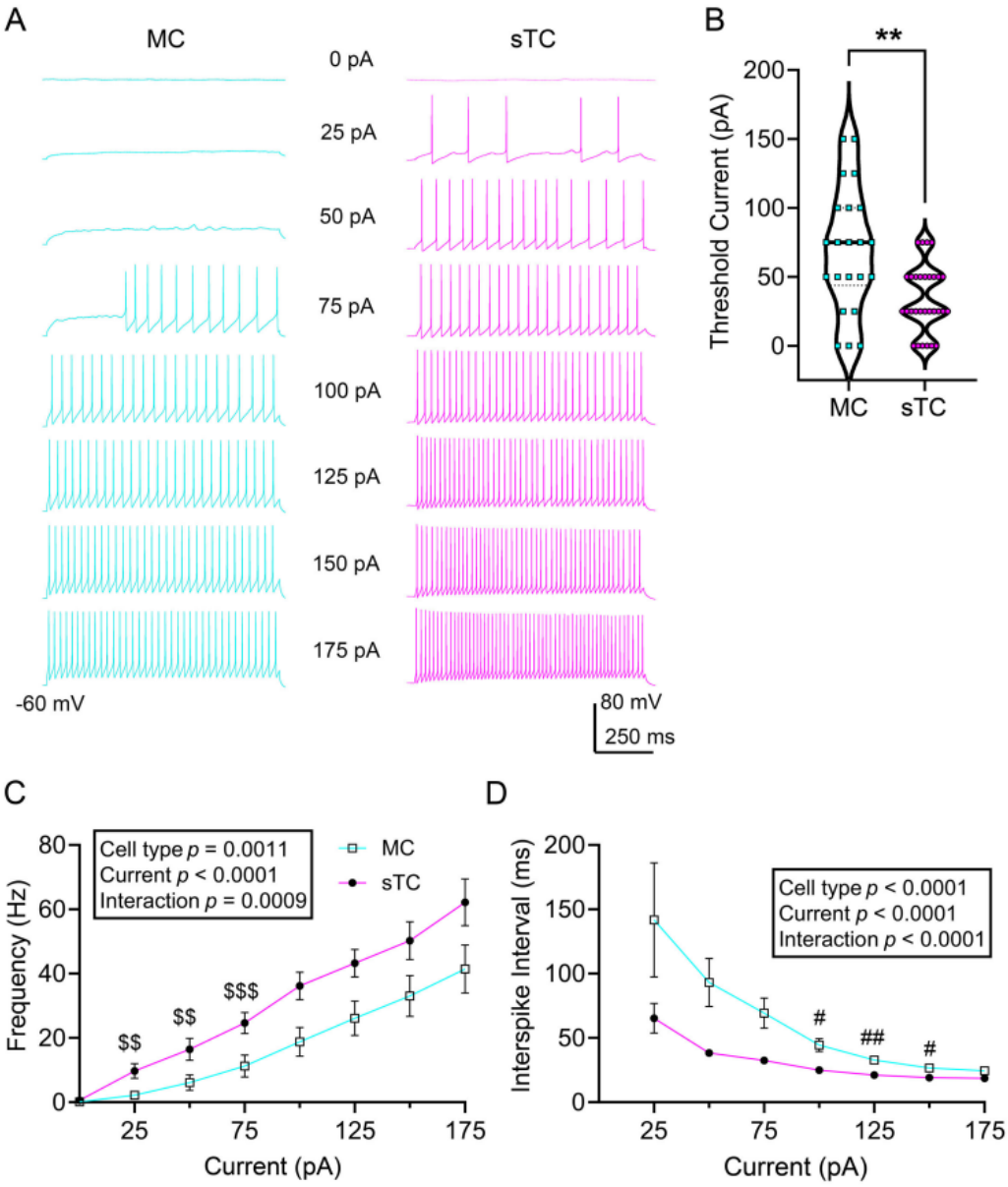

Fig. 4. Spike firing properties compared between mitral cells (MC) and superficial tufted cells (sTC). ***A*,** Representative action potential trains evoked by various current steps as indicated, recorded from a MC (***Left***) vs. sTC (***Right***). ***B*,** Violin plot comparing the current needed to evoke action potentials (rheobase), Mann-Whitney U, $^{**}p = 0.0021$. Line plots for ***C*,** mean spike frequency across current step and ***D*,** mean interspike interval (ISI). Line plot data were analyzed with a ***(C)*** 2-w mixed RM ANOVA, cell type $^{**}p = 0.0011$; current x cell type interaction $^{***}p = 0.0009$, Sidak's post-hoc test, $^{\$\$}p < 0.01$, $^{\$\$\$}p < 0.001$, ***(D)*** 2-w mixed RM ANOVA, cell type $^{****}p < 0.0001$; current x cell type interaction $^{****}p < 0.0001$, Sidak's post-hoc test, $^{\#}p < 0.05$, $^{\#\#}p < 0.01$.

327 Because potassium channel currents can greatly influence the characteristics of APs (**Fig. 2-**
328 **4**), we wanted to determine any differences in AP shape or kinetics that could accompany
329 these findings. Many AP parameters require a clearly defined baseline in order to be assessed
330 accurately, and the parameters are dependent on current injection magnitude. The metrics of
331 'maximum decay slope' and 'time to achieve maximum decay slope' are not dependent upon
332 correct identification of the recording baseline, and we therefore examined these metrics
333 simultaneously across all current injection steps. sTCs achieved steeper maximum decay
334 slopes than MCs, which also differed in a current-dependent manner (**Fig. 5A, C**). We applied
335 a 2-w mixed RM ANOVA using cell type and current step as factors. There was a main effect
336 of cell type (F (1, 50) = 5.914, $^{*}p = 0.0186$) and a current x cell type interaction (F (6, 127) =
337 5.562, $^{****}p < 0.0001$); a Sidak's post-hoc test indicated that cell-type significant differences
338 occurred at current steps 50 pA - $p^{\#\#\#} = 0.0006$, 75 pA - $^{\#\#\#\#}p < 0.0001$, and 100 pA - $^{\#\#}p =$
339 0.0074. APs recorded in sTCs also exhibited faster times to achieve maximum decay slope
340 than those in MCs, independent of current injection step (**Fig. 5B, C**). We applied a 2-w
341 mixed RM ANOVA using cell type and current step as factors. There was no effect of current
342 step (F (0.1425, 3.016) = 9.085, $p = 0.0524$), but there was a main effect of cell type F (1, 50)
343 = 4.088, $^{*}p = 0.0486$. A Sidak's post-hoc test, demonstrated that sTCs were faster at all
344 current injections at and above 75 pA (75 pA - $^{\#\#\#}p = 0.0002$, 100 pA - $^{\#\#}p = 0.0031$, 125 pA -
345 $^{\#}p = 0.0300$, 150 pA - $^{\#}p = 0.0274$).
346
347 Due to differences in excitability between MCs and sTCs (**Fig. 4**), the current injection step of
348 75 pA had the largest sample size for the comparison of AP characteristics that are dependent
349 upon verifiable baseline. Overall, we found that the APs of sTCs have greater peak
350 magnitude, greater antipeak (after-hyperpolarization) amplitude, faster rise kinetics, and faster
351 decay kinetics than MCs (**Table 1**). Mean values, sample sizes, *p* values, and statistical tests
352 are reported within each column.
353

	Peak Amplitude (mV)	Time to Peak Amplitude (ms)	Antipeak Amplitude (mV)	Time to Antipeak (ms)	Half Width (FWHM) (ms)
Mitral Cells	51.1 ± 10.0	5.83 ± 0.26	-12.1 ± 2.4	11.4 ± 0.7	1.78 ± 0.36
N	11	11	11	11	11
Superficial Tufted Cells	60.8 ± 7.0	5.72 ± 0.09	-15.1 ± 2.5	9.20 ± 0.90	1.32 ± 0.16
N	11	11	11	11	11
p-value	**0.0150**	ns (0.1970)	**0.0079**	**< 0.0001**	**< 0.0001**
Test used	†	†	⊤	†	⊤

	Max Rise Slope (mV/ms)	Time to Max Rise Slope (ms)	Max Decay Slope (mV/ms)	Time to Max Decay Slope (ms)	Rise Time to Half Amplitude (ms)
Mitral Cells	88.4 ± 35.2	5.11 ± 0.17	-44.3 ± 13.2	0.866 ± 0.167	5.09 ± 0.11
n	15	11	15	15	11
Superficial Tufted Cells	117.0 ± 44.0	5.06 ± 0.17	-79.5 ± 20.4	0.612 ± 0.105	5.11 ± 0.05
n	20	11	20	20	11
p-value	**0.0493**	ns (0.8338)	**< 0.0001**	**< 0.0001**	ns (0.7969)
Test used	†	⊤	‡	†	⊤

	Decay Time to Half Amplitude (ms)	Rise Slope 10% to 90% (mV/ms)	Rise Time 10% to 90% (ms)	Decay Slope 90% to 10% (mV/ms)	Decay Time 90% to 10% (ms)
Mitral Cells	6.87 ± 0.38	58.8 ± 24.1	1.04 ± 0.82	-31.3 ± 8.2	1.41 ± 0.21
n	11	11	11	11	11
Superficial Tufted Cells	6.43 ± 0.16	74.1 ± 18.3	0.784 ± 0.151	-56.7 ± 11.2	0.911 ± 0.107
n	11	11	11	11	11
p-value	**0.0021**	ns (0.1087)	ns (0.3192)	**< 0.0001**	**< 0.0001**
Test used	†	‡	†	‡	†

354 **Table 1.** Action potential shape compared between mitral cells (MCs) vs. superficial tufted cells
355 (sTCs). Recordings were made while holding cells near rest (V_h = -60 mV) and injecting 75 pA of
356 current. Values are mean ± standard deviation. ns = not significant, †= Student's *t*-test, ‡= *t*-test with
357 Welch's correction, ₸= Mann-Whitney U.

358

359 **Superficial tufted cells do not show a higher propensity to bursting activity**
360 **than mitral cells**

361 Previous reports demonstrate that MCs are less likely to exhibit trains of AP activity than TCs
362 in general (Liu and Shipley, 2008; Burton and Urban, 2014; Jones *et al*., 2020). As such, we
363 wanted to determine if this was also true of sTCs by applying further refined spike analysis.
364 After determining the supra-threshold current injection step, we injected cells at that threshold
365 using a P_d of 5000 ms and a T_s = 30 s for 10 total sweeps (**Fig. 5D**). We defined a "train" as
366 having 3 or more APs within a 100 ms period (Balu et al., 2004), and only directly compared
367 cells receiving identical current injection magnitude. sTCs did not exhibit more AP trains
368 within their respective recording periods (**Fig. 5E,** MCs = 28.7 ± 21.1 (7) AP trains vs. sTCs =
369 25.1 ± 21.3 AP trains (7), Student's *t*-test, p = 0.7582), nor did the trains of sTCs contain more
370 AP spikes (**Fig. 5F,** MCs = 10.8 ± 11.9 spikes/train (6) vs. sTCs = 11.3 ± 7.2 spikes/train (6),
371 Student's *t*-test, p = 0.2796). sTCs did not exhibit differing pause duration between trains
372 (**Fig. 5G,** MCs = 950 ± 890 ms (6) vs. sTCs = 1660 ± 1720 ms (6), Mann-Whitney U, p =
373 0.3939), nor a differing latency period to first spike (**Fig. 5H,** MCs = 327 ± 249 ms (6) vs.
374 sTCs = 535 ± 404 ms (7), Mann-Whitney U, p = 0.1375). To assess whether sTCs showed a
375 higher propensity to be a 'bursting cell' (as opposed to a regularly-firing cell), we assessed the
376 firing activity from all current-clamp recordings to determine the categorical type of each MC
377 and sTC. A cell was categorized as a "bursting cell" if any of its sweeps contained at least two
378 bursts separated by a pause duration of > 100 ms. sTCs did not show a statistically different
379 preference toward bursting or regularly firing than that of MCs (**Fig. 5I**, MCs = 28.6% (21),
380 sTCs = 40% (30), Chi-squared test, p = 0.40061, X^2 = 0.7065).

381

382

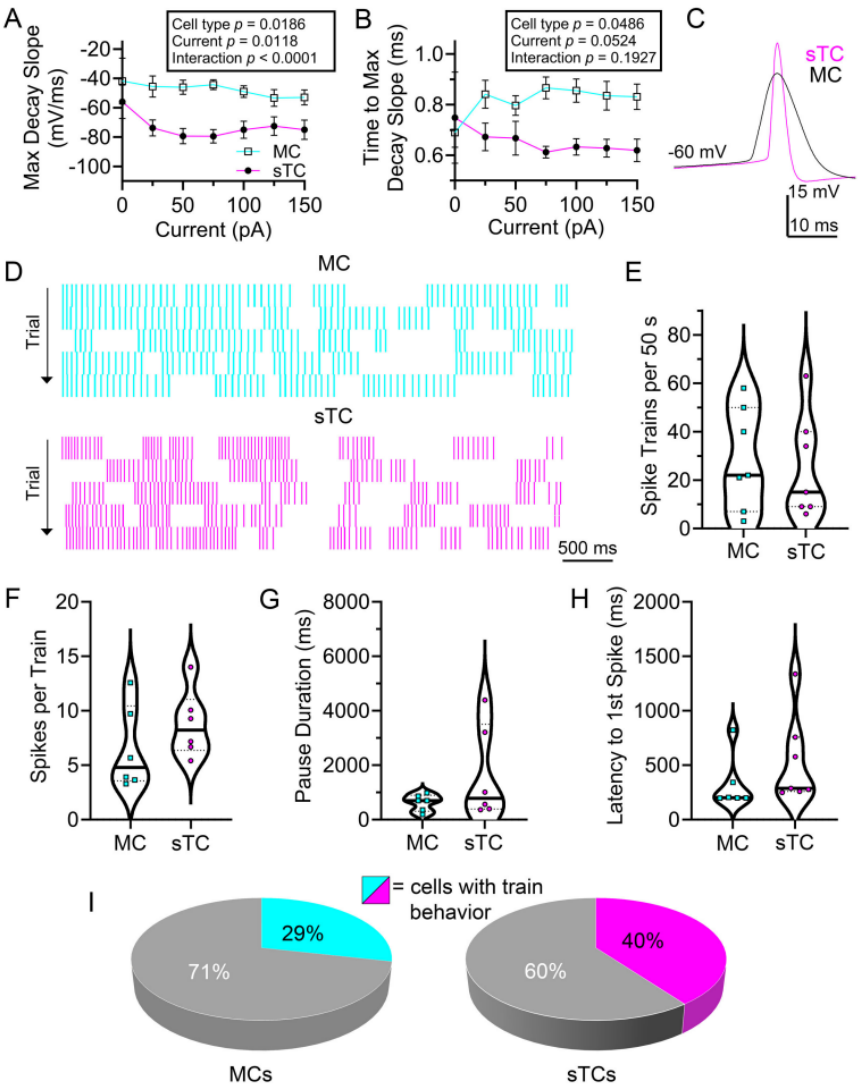

Fig. 5. Action potential shape and spike train activity compared between mitral cells (MC) and superficial tufted cells (sTC). Line plot for ***A,*** maximum decay slope (max decay slope) and ***B,*** time to achieve maximum decay slope from peak magnitude (time to max decay slope) across current step. Line plot data were analyzed with **(A),** 2-w mixed RM ANOVA, cell type *p = 0.0186, Sidak's post-hoc test, ##p < 0.01, ###p < 0.001; current x cell type interaction ****p < 0.0001, **(B),** 2-w mixed RM ANOVA, cell type *p = 0.0486, Sidak's post-hoc test, #p < 0.05, ##p < 0.01, ###p < 0.001. ***C,*** Representative pair of action potentials recorded in response to a 75 pA current injection held near rest (V_h = -60 mV). ***D,*** Representative raster plot for a cell stimulated with a 50-pA current injection using a P_d = 5 s for each cell type, respectively. Successive trials are stacked vertically below. Violin plots computed across a 50 s recording period (10, 5s sweeps) compare ***E,*** mean number of bursts, ***F,*** mean spikes per train, ***G,*** mean pause duration between trains, and ***E,*** mean latency to first spike. ***E-F,*** were analyzed using a Student's *t*-test, ***G-H*** were analyzed using Mann-Whitney U; $p > 0.05$. ***I,*** Relative proportion of cells eliciting spike train behavior among sampled MCs (***Left***) and sTCs (***Right***), respectively (Chi-squared test, p = .40061, $X^2 = 0.7065$, n = 51).

398

399 **Co-localization of Kv1.3 channel and the insulin receptor in superficial tufted**
400 **cells**

401

402 MCs are known be modulated by insulin, and Kv1.3 is necessary for this modulation (Fadool
403 and Levitan, 1998; Fadool et al., 2000, 2011; Tucker et al., 2010; Kuczewski et al., 2014). We
404 found sTCs to be modulated by margatoxin (**Fig. 3**), suggesting expression of Kv1.3. We
405 therefore performed immunocytochemistry to determine co-expression of Kv1.3 and the
406 insulin receptor (IR) in sTCs, similar to what we have observed for MCs (Marks and Fadool,
407 2007; Colley et al., 2009; Marks et al., 2009; Thiebaud et al., 2016). Using the GFP mice
408 (Tbx21/Cas9/GFP), we observed the GFP-label localized to the M/TCs neurolamina (**Fig. 6A**,
409 MCL and EPL, blue arrow MCs and orange arrow sTCs) as previously reported for this
410 reporter line (Kolling et al., 2022). A majority of these neurons demonstrated expression of
411 Kv1.3 channel and IR kinase (**Fig. 6B, 6C**) that was co-localilzed (**Fig. 6D**, white arrowhead)
412 and overlayed with the GFP expression (merge, **Fig. 6E**). Correlated, higher magnification
413 images were acquired to resolve the expression patterns and co-expression at the single
414 neuron level (mitral cells **Fig. 6A1-E1**, superficial tufted cells **Fig. 6A2-6E2**).
415 Using Kv1.3-/- mice as a negative control for channel expression and co-localization with IR
416 kinase, we observed that the prominent detection of individual protein label and co-expression
417 patterns observed in the MCL, EPL, and GCL of wildtype mice (**Fig. 6F**), were absent in
418 Kv1.3-/- mice (**Fig. 6M**). Higher magnification images showing labeling in wildtype mice
419 (mitral cells **Fig. 6G-I**; superficial tufted cells **Fig. 6J-L**) vs. that of Kv1.3-/- mice (mitral
420 cells **Fig. 6N-P**; superficial tufted cells **Fig. 6Q-S**) further resolved the lack of signal for the
421 Kv1.3 channel. These data indicated that loss of Kv1.3 channel did not grossly affect
422 expression patterns of IR kinase. To further confirm the retention of IR kinase expression
423 patterns in sTC following loss of Kv1.3 expression, we examined GFP mice following
424 CRISPR-mediated deletion of Kv1.3 channel in M/TCs (**Fig. 6T-6X**). Indeed, sTCs that had
425 been CRISPR-edited – expressing Cas9 (**Fig. 6U**) and taking up sgRNA (**Fig. 6W),** continued
426 to express IR kinase (**Fig. 6V**) in the absence of Kv1.3 channel (merge low power **Fig. 6T**,
427 high magnification **Fig. 6X**).

428

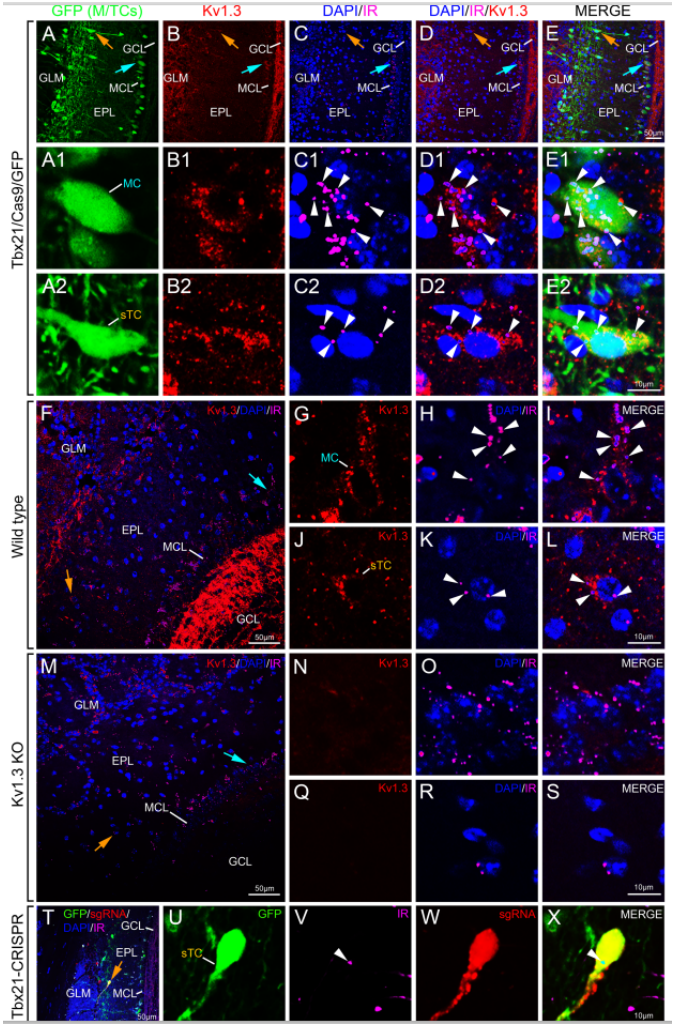

Fig. 6. Colocalization of the Kv1.3 channel (Kv1.3) and the insulin receptor (IR) in superficial tufted cells (sTCs) and mitral cells (MCs) using double-color immunofluorescence confocal microscopy. Photomicrographs demonstrating Kv1.3- and IR-immunoreactivity in GFP mice (Tbx21/Cas9/GFP mice). ***A-E,*** Representative olfactory bulb slice at lower magnification indicating ***A,*** endogenous EGFP (GFP) selective in Tbx21 x Cas9 lines (green) ***B,*** Kv1.3 (red), ***C,*** IR (pink) and DAPI (blue) nuclear stain, and ***D,*** co-localization of Kv1.3 + IR, ***E,*** merge to GFP signal. ***A1-E1,*** Representative MC and ***A2-E2,*** representative sTC at higher magnification. GLM = glomerular layer, EPL= external plexiform layer, MCL = mitral cell layer, GCL: granule cell layer. Light blue arrow = MCL, orange arrow = sTCs near adjacent EPL, white arrowhead = Kv1.3 + IR co-labeled neuron. Representative photomicrographs demonstrating Kv1.3- and IR-immunoreactivity in ***F,*** wildtype and ***M,*** Kv1.3-/- mice. ***G-I,*** Representative MC and ***J-L,*** representative sTC at higher magnification for wildtype mice in comparison with a ***N-P,*** MC and a ***Q-S,*** sTC for Kv1.3-/- mice. Abbreviations and notations the same as (**A-E2**). ***T-Y,*** Representative photomicrographs demonstrating IR-immunoreactivity following CRISPR editing of Kv1.3 channel (Tbx21-CRISPR). ***U,*** Endogenous EGFP (GFP) selective in Tbx21 x Cas9 lines, ***V,*** IR, ***W,*** sgRNA, ***X,*** higher magnification of a sTC, merge to GFP signal and ***T,*** associated low power of identical field of view. Abbreviations and notations the same as (**A-E2**).

446

447 We next performed multiplex fluorescent *in situ* hybridization (RNAscope) to determine co-
448 expression of Kv1.3 and the insulin receptor (IR) in sTCs as a secondary confirmation with
449 resolution at the molecule level to include quantification. Using a transgenic GFP label for
450 M/TCs under control of the *Tbx21* promoter, we performed RNAscope targeting *Kv1.3*, *GFP*,
451 and *Insr* on six coronal sections sampled 512 µm apart along the antero-posterior axis (AP
452 axis), in both male and female mice. We observed co-localization of the channel and the
453 receptor markedly distributed with the expression of the *Tbx21* promoter by imaging at low
454 power across the entire olfactory bulb (**Fig 7A-D**). We then moved to higher magnification in
455 the EPL to visualize the sTC specifically, and the colocalization of the channel and receptor
456 with the *Tbx21* reporter expression (**Fig. 7E-H**). A 2-way comparison revealed a main effect
457 of AP axis on Tbx21+ cell count (**Fig. 7I**, *p = 0.0118) with no interactive effect of axis on
458 sex or laminar layer (p = 0.3020; M MCL, M EPL, M GLM, F MCL, F EPL, F GLM as
459 columns variables; M = male, F = female). We then examined the percentage of Tbx21+ cells
460 co-labeled with both *Kv1.3* and *Insr* along the antero-posterior axis, and found no main effect
461 of AP axis (**Fig. 7,** p = 0.5736) or interactive effects on sex or laminar layer (p = 0.7359).
462 Without regard for antero-posterior position or sex (since these were not found to be factors
463 for co-labeling), we assessed the percentage of Tbx21+ cells that express both *Kv1.3* and *Insr*.
464 We find triple-labeling of 82.1 $\pm$ 4.3 % in the MCL, 73.4 $\pm$ 8.2 % in the EPL, and 76.2 $\pm$ 6.8
465 % in the GLM. ANOVA comparisons across neurolaminae revealed a subtle difference in the
466 percentage of all Tbx21+ cells expressing *Kv1.3* alone (**Fig. 7K**, *p = 0.0159) and expressing
467 both *Kv1.3* and *Insr* (**Fig. 7M**, *p = 0.0373).

468
469
470
471
472
473
474
475
476

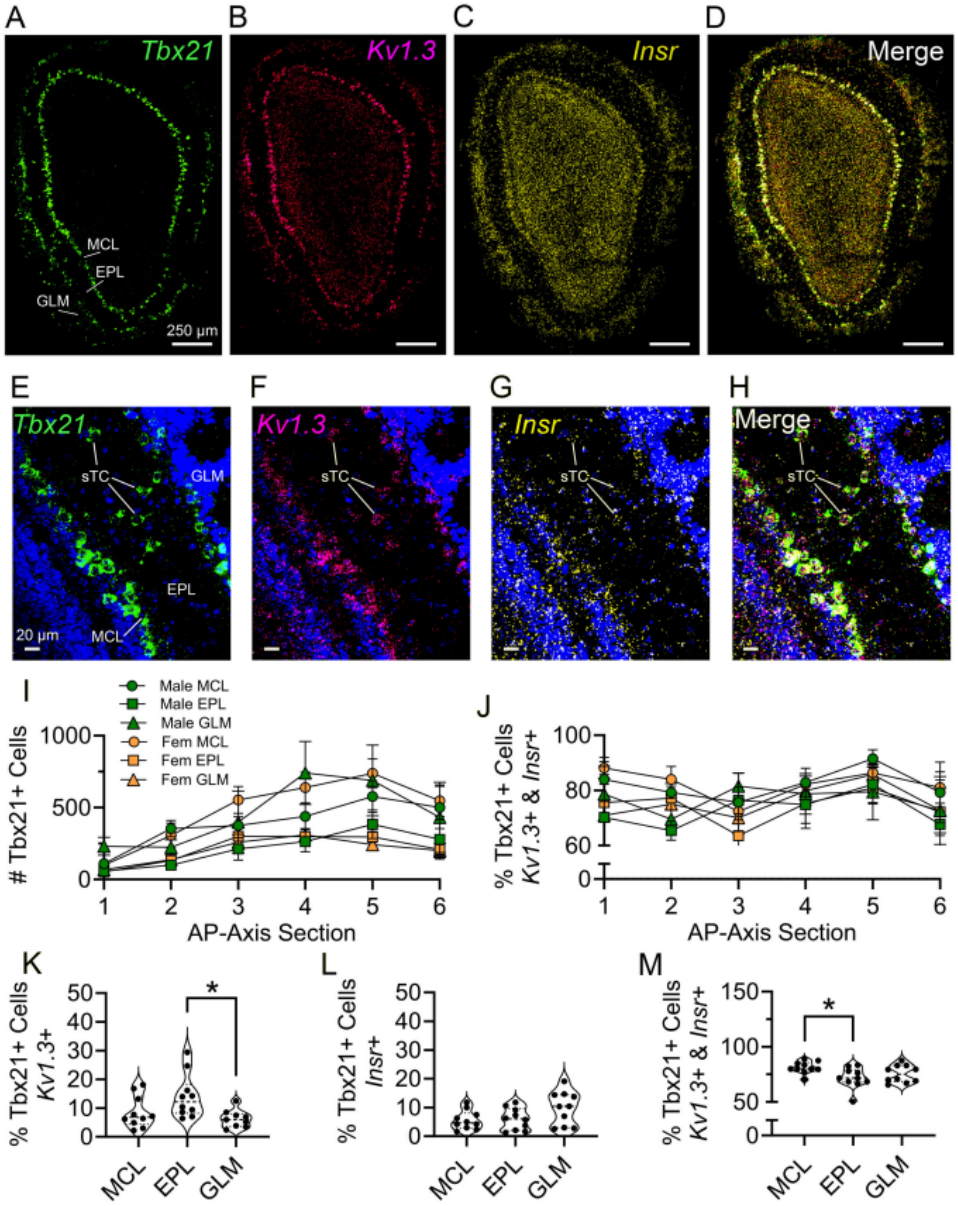

Fig. 7. Colocalization of MCs/sTCs with the Kv1.3 channel (*Kv1.3*) and insulin receptor (*Insr*) using RNAscope. Photomicrographs demonstrating neurolaminar distribution of Tbx21 reporter expression (green, ***A***), *Kv1.3* expression (magenta, ***B***), and *Insr* expression (yellow, ***C***), separately and merged (white, ***D***). ***E–H***: Same as ***A–D***, but to demonstrate localization to sTCs with the inclusion of a DAPI nuclear stain. ***I:*** Coronal sections were sampled along the anter-posterior axis (AP axis) at ~512 µm intervals and assessed for total number of M/sTCs (Tbx21+ cells) and for percentage of M/sTCs expressing both *Kv1.3* and *Insr* (***J***). Each data point represents the average from 5 separate mice, separated by laminar layer and sex. ***K–M:*** Percentage of M/TCs (Tbx21+ cells) expressing *Kv1.3* alone (***K***), *Insr* alone (***L***) or both (***M***). Statistical comparisons for ***K–M*** are Kruskal-Wallis (ANOVA) with Dunn's multiple comparisons test. Each data point represents the average of all six antero-posterior sections from each mouse, one data point per mouse per neurolaminar layer, respectively. $^{*}p < 0.05$, GLM = glomerular layer, EPL = external plexiform layer, GCL = granule cell layer.

489

490 **Superficial tufted cells are modulated by insulin via the Kv1.3 ion channel**

491 To further explore the complementary physiological role of sTCs, we wanted to determine if
492 their excitability could be modulated by insulin—knowing that MCs are modulated by 0.1 μm
493 insulin (Fadool *et al*., 2000, 2011). After sampling for supra-threshold current, synaptic
494 blockers were added to the bath solution. Evoked APs were established using the threshold
495 current with a P_d = 5000 ms and T_s = 30 s for a 5-min paradigm (10 recordings). A
496 representative set of baseline recordings and an associated raster plot is shown in **Fig. 8A,**
497 prior (left) and subsequent (right) to bath application of insulin for 15 min.

498

499 Insulin significantly reduced the average latency to first spike by ~38% (**Fig. 8B**, sTC pre =
500 1220 ± 723 ms (11) vs. sTC post = 649 ± 403 ms (11), paired *t*-test, **p* = 0.0132). On average,
501 insulin also increased the AP frequency by ~98% (**Fig. 8C**, sTC pre = 4.76 ± 1.76 Hz (11) vs.
502 sTC post = 8.49 ± 4.98 Hz (11), paired *t*-test, **p* = 0.0381), and decreased the average
503 intraburst interval by ~8% (i.e., the pause between APs within a particular burst) (**Fig. 8D**,
504 sTC pre = 65.1 ± 13.6 ms (11) vs. sTC post = 60.3 ± 14.9 ms (11), paired *t*-test, **p* = 0.0136).
505 All statistical tests were performed on non-normalized data, however, plots were generated as
506 normalized paired values to visualize individual cell changes across the sampled cells.

507

508 The modulation of MCs by insulin has been shown to depend on the Kv1.3 ion channel using
509 either pharmacological block or targeted gene-deletion (Fadool *et al*., 2000, 2011; Colley *et*
510 *al*., 2004). Since previous reports demonstrate Kv1.3 expression in sTCs (Kues and Wunder,
511 1992; Fadool *et al*., 2000; Colley *et al*., 2007), we wanted to determine if insulin modulation
512 of sTCs was also Kv1.3-dependent. Using transgenic mice lacking the *Kv1.3* gene (Kv1.3-/-,
513 see methods) we first compared the AP bursting characteristics between the sTCs of GFP
514 mice (Kv1.3 +/+), and the sTCs of Kv1.3 -/- mice. In accordance with the findings in Kv1.3 -
515 /- MCs (Fadool *et al*., 2004, 2011; Tucker *et al*., 2010; Thiebaud *et al*., 2016), we found that
516 Kv1.3 -/- sTCs tend to burst more often, and have shorter bursts with faster intraburst
517 frequency. Kv1.3 -/- sTCs also have shorter latency to first spike and faster overall evoked AP
518 frequency than Kv1.3 +/+ sTCs (**Table 2**). Mean values, sample sizes, *p* values, and statistical
519 tests are reported within each column.

	Bursts per 50 s (n)	Spikes per Burst (n)	Burst Duration (ms)	Intraburst Interval (ms)	Intraburst Frequency (Hz)
Kv1.3 +/+ sTCs	24.8 ± 10.0	7.6 ± 3.1	414.6 ± 209.5	65.1 ± 12.9	17.0 ± 5.6
n	11	11	11	11	11
Kv1.3 -/- sTCs	55.0 ± 9.6	6.0 ± 1.4	215.0 ± 82.4	45.6 ± 11.7	26.1 ± 8.7
n	4	4	4	4	4
p-value	**0.0003**	ns (0.2362)	**0.0305**	**0.0291**	**0.0048**
Test used	†	‡	‡	†	₸

	Pause Duration (ms)	Latency to First Spike (ms)	AP Frequency (Hz)	Event Frequency (Hz)	% Bursting Cells
Kv1.3 +/+ sTCs	729.8 ± 354.1	1221.6 ± 689.4	4.8 ± 1.7	7.6 ± 2.6	
n	11	11	11	11	
Kv1.3 -/- sTCs	655.3 ± 210.4	419.5 ± 298.7	7.1 ± 2.2	7.6 ± 2.5	
n	4	5	5	5	
p-value	ns (0.7183)	**0.0090**	**0.0475**	ns (0.7427)	
Test used	†	‡	†	₸	

Table 2. Spike bursting properties in superficial tufted cells (sTCs) compared between wildtype (WT) and Kv1.3 -/- mice. Recordings were made while holding cells near rest (V_h = -60 mV) and injecting 75 pA of current. Data were computed across a 50 s recording period (10, 5s sweeps). Values are mean ± standard deviation. ns = not significant, †= Student's *t*-test, ‡= *t*-test with Welch's correction, ₸= Mann-Whitney U

Using Kv1.3 -/- mice, we next repeated the previous insulin experiment shown **Fig. 8A** representative set of baseline recordings and associated raster plot for sTCs evoked APs is shown in **Fig. 8E**, prior (left) and subsequent (right) to bath application of insulin for 15 min as recorded in the Kv1.3-/- mice. Unlike in recordings acquired from Kv1.3 +/+ mice, insulin

did not alter latency to first spike (**Fig. 8F**, Kv1.3-/- sTC pre = 420 ± 334 ms (5) vs. Kv1.3-/- sTC post = 390 ± 232 ms (5), paired *t*-test, $p = 0.5694$). Insulin also did not affect AP firing frequency (**Fig. 8G**, Kv1.3-/- sTC pre = 7.09 ± 2.48 Hz (5) vs. Kv1.3-/- sTC post = 7.13 ± 2.93 Hz (5), paired *t*-test, $p = 0.9300$, n = 5), nor affect the intraburst interval (**Fig. 8H**, Kv1.3-/- sTC pre = 45.6 ± 13.6 ms (4) vs. Kv1.3-/- sTC post = 52.7 ± 17.8 ms (4), paired *t*-test, $p = 0.1990$, n = 4) in Kv1.3-/- mice. The same 5 cells were used for all pre/post comparisons, but one cell did not fire quickly enough for burst analysis (see methods).

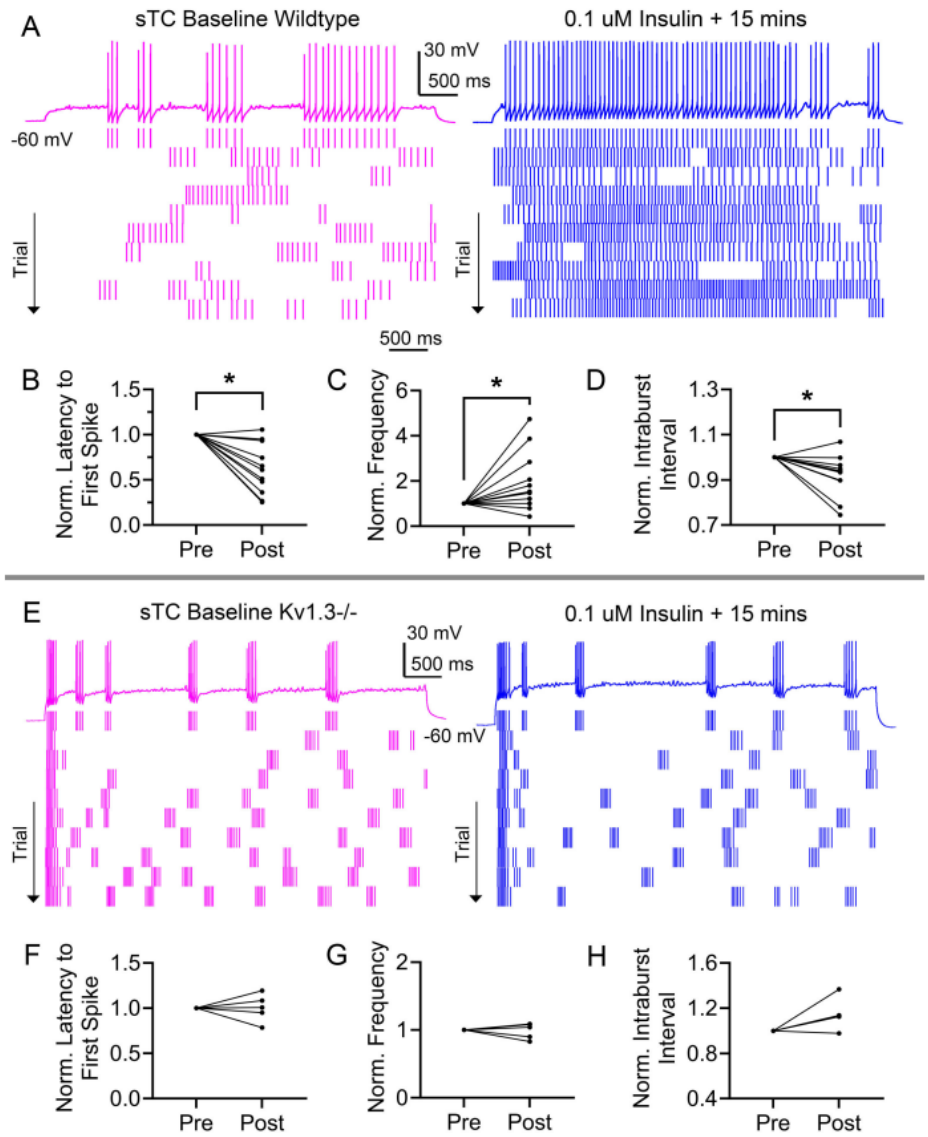

Fig. 8. Bath application of insulin increases spike firing frequency, and shortens latency to first spike and intraburst interval in superficial tufted cells (sTCs) in wildtype mice (***A-D***), but fails to do so in superficial tufted cells in Kv1.3-/- mice (***E-H***). ***A,*** Representative spike trains (***Top***) that were elicited in response to 25 pA current injection while holding the cell near rest (V_h = -60 mV) prior (***Left,*** Baseline) and subsequent (***Right,*** Insulin) to hormone stimulation using P_d = 5 s. (***Bottom***) Representative associated raster plot. Line graph comparing ***B,*** latency to first spike, ***C,*** spike firing frequency, and ***D,*** intraburst interval, prior (pre) and following (post) insulin stimulation in the same cell. Data were analyzed with a paired *t*-test using non-normalized data ***(B)*** $*p = 0.0132$, ***(C)*** $*p = 0.0381$, and ***(D)*** $*p = 0.0136$. ***E,*** Representative spike trains (***Top***) and associated raster plot (***Bottom***) recorded as in *Panel A,* but in Kv1.3-/- mice. Line graph comparing ***F,*** latency to first spike, ***G,*** spike firing frequency, and ***H,*** intraburst interval, prior (pre) and following (post) insulin stimulation in the same cell. Data were analyzed with a paired *t*-test using non-normalized data, $p > 0.05$.

574

575 ## Discussion

576 We have demonstrated that the two major output neurons in the olfactory bulb have different
577 biophysical properties, despite both neurons expressing IR kinase and exhibiting modulation
578 by insulin. sTCs are more excitable, as evidenced by the lower threshold needed to evoke an
579 AP, a decreased ISI, and a greater AP firing frequency particularly at lower current injection.
580 We found that the APs of sTCs have greater peak amplitude, greater anti-peak amplitude,
581 faster rise kinetics, and faster decay kinetics than those of MCs – while at the same time, the
582 incidence of a train of AP activity was similar between the two output neurons. While there
583 are differences in the voltage dependence of voltage-activated outward currents between MCs
584 and sTCs, both are blocked by the Kv1.3 vestibule blocker, MgTx. We determined that
585 voltage-activated outward currents in sTCs are modulated by insulin, and that the Kv1.3 ion
586 channel is necessary for this modulation.
587
588 Burton and Urban (Burton and Urban, 2014) first compared mitral cell biophysical properties
589 with that of what they called "tufted cells", which were projection neurons whose cell bodies
590 resided in the superficial 50% of the EPL. Prior to their publication, physiologists often
591 clustered mitral and tufted cells together as a homogenous neuronal population (Fadool and
592 Levitan, 1998; Tucker and Fadool, 2002; Youngstrom and Strowbridge, 2015; Liu et al.,
593 2016) due to their similar function as output neurons. Using new nomenclature described by
594 Jones et al. (Jones et al., 2020), we now know that TCs are comprised of a variety of sub-
595 classes that are functionally distinct with differential sensitivity to inhibitory/excitatory
596 circuits to putatively sharpen tuning specificity for odorants during sensory processing (Zhou
597 et al., 2023). We also know from transcriptome and RNA sequencing studies that there are
598 multiple subclasses of each of these projection neurons based upon molecular determinants
599 (Zepelli et al., 2021). The tufted cells first measured by Burton and Urban (2014) likely
600 consisted of a mixed population of sTCs and mTCs. Nonetheless, some of our data measured
601 in strictly sTCs, align well with what they reported for "tufted cells" in general. Burton and
602 Urban found that their TCs had a higher instantaneous frequency (peak instantaneous rate)
603 that differed with current injection magnitude than that of MCs, and that the AP shape of their
604 TCs exhibited a narrower half width (FWHM), a steeper decay slope, and faster time to anti-

605 peak (after-hyperpolarization). Our comparative measurements were quite similar. Thus, we
606 similarly report that sTC have greater intrinsic excitability than that of MCs. Unlike this
607 earlier study, however, we found that the AP shape in sTCs compared with that of MCs, has a
608 greater peak amplitude, steeper maximum rise slope, a greater anti-peak amplitude, and the
609 minimum current necessary to evoke a first AP (threshold) is lower.
610
611 Burton and Urban further found that their TCs were more likely to elicit spike trains (stutter)
612 compared with that of MCs, which they characterized based upon the increased co-efficient of
613 variation of the ISI observed in the TCs. We did not observe a greater overall firing
614 irregularity in our recorded sTCs, and in fact, we found the opposite - our recorded MCs had a
615 greater ISI variance at lower levels of current injection than that of sTC. Also inconsistent
616 with our findings; sTCs and MCs did not have significantly different AP train properties
617 (spikes per train, pause duration, or latency to first spike), nor did sTCs have a statistically
618 higher propensity to elicit a spike train. The likely inclusion of both sTCs and mTCs in their
619 study could account for these differential findings. In fact, Antral et al. (2006) also reports in
620 their study of eTC, that they observed two subclassifications, nonbursting (contained lateral
621 dendrites) and bursting (lacked lateral dendrites), that were found to be both morphologically
622 and functional diverse. We believe that we have complemented the findings of Burton and
623 Urban, expanding upon their comparisons to more specifically characterize selectively the
624 sTCs and not multiple subtypes clustered together.
625
626 Differences in ion channel expression could underlie the greater excitability of sTCs
627 compared to that of MCs. We found voltage-activated currents in the window of -60 to -20
628 mV to be greater in MCs than those of sTCs. It is well known that *shaker* family members
629 have a voltage-activation above -50 to -40 mV (Zagotta and Aldrich, 1990), therefore Kv1.2
630 and Kv1.3 likely are not highly responsible for the difference in voltage-activated currents
631 between the two cell types. This is corroborated by the fact that both cell types exhibited a
632 similar pharmacological response to MgTx and both are shown to be similarly modulated by
633 bath application of insulin, previously demonstrated to be the result of Kv1.3 being used as a
634 substrate for tyrosine phosphorylation in the OB in a use- or activity-dependent manner
635 (Fadool et al., 2000, 2011). We also measured a select slowing of the deactivation kinetics in

636 MCs at the sampled -40 mV hyperpolarizing step that might selectively lower MC excitability
637 vs. that in sTCs. A comparison of MC activity in Kv1.3-/- mice vs. pharmacological block of
638 the channel in the current study, may reveal differences in underlying ion channel expression
639 between sTCs and MCs. The threshold for activation of voltage-activated outward currents in
640 the MCs of Kv1.3-/- mice were previously found to be shifted +20 mV in the positive
641 direction compared to wild-type MCs (Fadool et al., 2004), but these Kv1.3-/- MCs have an
642 upregulation of a *slack* sodium-activated potassium (K_{Na}) channel (Lu et al., 2010), an
643 increase in calcium channel expression (Fadool et al., 2004), and may have increased chloride
644 currents (Koni et al., 2003). Therefore, the threshold for activation of voltage-activated
645 currents in sTCs and Kv1.3-/- MCs is both higher than that of wildtype MCs, but the precise
646 nature of any differences in channel expression (i.e., perhaps sTCs express higher levels of
647 K_{Na} channels than MCs) is not known. One study that has tried to address differential
648 expression of voltage-gated K channels across MC and TCs, in general, is that of Zeppilli et
649 al. (2021). These authors have demonstrated distinct RNA expression levels of Kcnd3,
650 Kcng1, Kcnh5, Kcnq3, Kcnj2 and 6, and Hcn1 that may represent candidates for controlling
651 the differential excitability of different MC and TC subtypes. This opens the door to a larger
652 area of research that is beyond the scope of this report.
653
654 sTCs are modulated by the presence of insulin, and our data demonstrate that this modulation
655 depends upon the Kv1.3 ion channel. Insulin's primary role in the periphery is to mobilize
656 glucose from the bloodstream following a meal; however, insulin is known to have many roles
657 as a signaling molecule in the central nervous system (CNS). The levels of insulin in the CNS
658 do not mirror the levels of insulin in the periphery, and the highest concentration of insulin
659 receptors and binding affinity to insulin (outside the pancreas) is found in the OB (Baskin et
660 al., 1983; Hill et al., 1986; Gupta et al., 1992; Schwartz et al., 1992; Myers Jr. and White,
661 1993; White, 1997; Wickelgren, 1998; Banks et al., 1999; Fadool et al., 2000; Aimé et al.,
662 2012; Palouzier-Paulignan et al., 2012; Fadool and Kolling, 2020). MCs have an interesting
663 co-localization of IR kinase and Kv1.3 with adaptor proteins that functions to cluster signaling
664 transduction cascades in close proximity (Marks and Fadool, 2007; Marks et al., 2009). In the
665 brain, insulin resistance is implicated in the progression of neurodegeneration and dementia
666 (Kuljiš and Salković-Petrišić, 2011; Arnold et al., 2018; Ferreira et al., 2018; Hong et al.,

667 2021; Femminella et al., 2021). Our report elevates the role of Kv1.3 as a target for the
668 investigation of olfactory function, and, by extent, the complexities of insulin signaling in the
669 OB. Though not annotated directly, previous histological reports suggested expression of
670 Kv1.3 in sTCs. These include Figure 1E from Kues 1992 (Kues and Wunder, 1992), Figure 7
671 from Fadool 2000 (Fadool et al., 2000), and Figure 9 from Colley 2007 (Colley et al., 2007).
672 At this time, we do not know of any reports that previously suggested expression of insulin
673 receptors on sTCs. MCs are known to be modulated by insulin in a similar manner to our sTC
674 findings (Fadool et al., 2000, 2011; Das et al., 2005; Tucker et al., 2010; Aimé et al., 2012;
675 Kuczewski et al., 2014), and this modulation in MCs is known to occur via phosphorylation of
676 Kv1.3 (Bowlby et al., 1997; Fadool and Levitan, 1998; Fadool et al., 2000, 2011).
677
678 Tbx21-cre lines have been previously utilized to selectively label M/TCs and delineate
679 downstream olfactory pathways (Mitsui et al., 2011; Kolling et al., 2022). Herein, we utilized
680 this line to parse out the TC subtypes based on their position in the neurolamina.
681 Juxtaglomerular eTCs situated at the periphery of the glomeruli could be clearly distinguished
682 from sTCs situated along the outer two thirds of the EPL (Jones et al., 2020). An
683 autoradiographic insulin binding study (Hill et al., 1986) and *in situ* hybridization analyses
684 (Marks et al., 1990) have confirmed the high density of insulin receptor expression across
685 different layers of olfactory bulb. In agreement with our current immunocytochemical data,
686 Aime et al. (2012) demonstrated the highest density of IR kinase specifically in the mitral
687 cells of rats. We observed that the number of IR-immunoreactive puncta was higher in
688 number and density in the MCL compared to that of the adjacent EPL and GLM.
689 Interestingly, we could use the Tbx21-cre lines to visualize sTCs that expressed IR, and noted
690 that the density of IR punta in sTCs was comparatively lower than that observed in MCs.
691 Although we did not examine the mechanism by which insulin might regulate sTCs, it is
692 predicted that Kv1.3 is a substrate for insulin-mediated phosphorylation (Fadool et al., 2000;
693 2011), which is in keeping with co-localization of the channel and the kinase in both MCs and
694 sTCs. We note that despite reported signaling interaction between channel and kinase (Marks
695 and Fadool, 2007; Marks et al., 2009), and the fact that modulation of spike firing frequency
696 in sTCs was dependent upon the presence of Kv1.3 channel, IR expression was retained in
697 both Kv1.3-/- and CRISPR-edited mice. While we do not know if the general insulin

698 signaling pathway is perturbed in the absence of Kv1.3, expression of the receptor appears to
699 be independent of the channel, and reciprocally, insulin modulation of the projection neurons
700 is dependent upon the channel. In agreement with prior physiological findings (Tucker et al.,
701 2010), Kv1.3-/- mice, lacking Kv1.3 immunoreactivity, also do not hamper the expression of
702 IR across different OB layers.
703
704 While we know that IR kinase is also co-localized with glucagon-like 1 peptide receptors in
705 MCs (Thiebaud et al., 2016) and have discovered an array of neuromodulators that alter Kv1.3
706 channel function and general excitability of these output neurons (Cook and Fadool, 2002;
707 Tucker and Fadool, 2002; Colley et al., 2009; Fadool et al., 2011; Mast and Fadool, 2012;
708 Tucker et al., 2013; Huang et al., 2017; Thiebaud et al., 2019), the possibility of
709 neuromodulation of sTCs remains highly likely and greatly unexplored. Herein, we have
710 distinguished these two output neurons in terms of biophysical function, but there may be a
711 range of neuromodulators that can affect and fine tune odor information coding or regulation
712 of metabolic state (Thiebaud et al., 2016, 2019; Kolling et al., 2022). Moreover, we have
713 recently enhanced total excitability of the output neurons (MCs and all classes of TCs) using
714 cell selective CRISPR genome editing of Kv1.3 to support a new function of the olfactory
715 system – metabolic regulation and energy homeostasis (Kolling et al., 2022). Thus, there is
716 much to discover concerning both the division of olfactory function between MCs and TCs
717 (odor context, valence, vs. odor identity), as well as the combined parallel function of
718 olfactory output neurons in regulating whole-body metabolism.
719

720 # MATERIALS AND METHODS

721 ## Ethical approval

722 All animal procedures were reviewed and approved by Florida State University (FSU)
723 Laboratory Animal Resources (Protocol 202000045) that abided by the American Veterinary
724 Medical Association (AVMA) and the National Institutes of Health (NIH). In preparation for
725 OB slice electrophysiology, mice were anesthetized with isoflurane (Aerrane; Baxter,
726 Deerfield, IL, USA) using the Institutional Animal Care and Use Committee (IACUC)-
727 approved drop method and then were killed by decapitation (AVMA Guidelines on
728 Euthanasia, June 2007). In preparation for histology, mice were anaesthetized with a mixture

729 of ketamine (100 mg/kg body weight) and xylazine (10 mg/kg body weight) prior to
730 intracardial perfusion with 4% paraformaldehyde and euthanasia by decapitation (AVMA
731 Guidelines on Euthanasia, June 2007). Our work was guided by the animal ethics checklist
732 reported by Grundy, 2015 (Grundy, 2015).
733

734 **Solutions and reagents**

735 Salts and sugars, unless otherwise noted, were obtained from Thermo Fisher Scientific
736 (Waltham, MA, USA) or Sigma-Aldrich Chemical (St. Louis, MO, USA). Artificial cerebral
737 spinal fluid (aCSF) contained (in mm): 119 NaCl, 26.2 $NaHCO_3$, 1 NaH_2PO_4, 2.5 KCl, 1.3
738 $MgCl_2$, 2.5 $CaCl_2$ and 22 d-glucose (pH 7.3; 300–310 mOsm). Sucrose-modified aCSF was
739 used for vibratome sectioning and recovery, and contained (in mm): 83 NaCl, 26.2 $NaHCO_3$,
740 1 NaH_2PO_4, 3.3 $MgCl_2$, 0.5 $CaCl_2$, 72 sucrose and 22 d-glucose (pH 7.3; 300-310 mOsm) (Jan
741 and Westbrook, 2007). Slice intracellular (pipette) solution contained (in mm): 135 potassium
742 gluconate, 10 KCl, 10 HEPES (N-2-hydroxyethylpiperazine-N-2-ethane sulfonic acid), 10
743 $MgCl_2$, 0.4 NaGTP and 2 NaATP (pH 7.3; 280–285 mOsm). PBS contained the following (in
744 mm): 136.9 NaCl, 2.7 KCl, 10.1 Na_2HPO_4, and 1.8 KH_2PO_4 (pH 7.4). Paraformaldehyde
745 (PFA) for tissue fixation consisted of 4% PFA (Eastman Kodak, Rochester, NY, USA) in
746 PBS. Blocking buffer and incubation buffer consisted of 2% bovine serum albumin fraction V
747 (BSA) (Invitrogen, Waltham, MA, USA) and 0.2% Tween-20 (Fisher, Hampton, NH, USA)
748 in 1X PBS (Salameh et al., 2017).
749

750 The following synaptic blockers and channel vestibule blocker were prepared as concentrated
751 stock solutions in aCSF, stored at -20ºC until day of use, and then diluted to the following
752 working concentrations: 10 µM gabazine (catalog #104104-50-9, MilliporeSigma, Burlington,
753 MA, USA), 5 µM 2,3-dioxo-6-nitro-7-sulfamoyl-benzo[f]quinoxaline (NBQX, catalog
754 #ab120045, Abcam, Waltham, MA, USA), 25 µM (2R)-amino-5-phosphonovaleric acid (AP5,
755 catalog #ab120003, Abcam), 1 nM margatoxin (MgTx, catalog # M8278, MilliporeSigma),
756 0.1 uM insulin (Fadool et al., 2011*a*) (catalog #I2643, MilliporeSigma), and 100 nM
757 tetrodotoxin (TTX, catalog # 120055, Abcam). Prior to use, MgTx and insulin were
758 additionally mixed with 0.05% bovine serum albumin (BSA fraction V, catalog # BSAV-RO,
759 Sigma-Aldrich) to prevent loss of peptide to tubing and plasticware while recording.

760

761 **Antibodies**

762 Monoclonal antibodies targeting the beta subunit of the IR or green fluorescent protein were
763 purchased from Santa Cruz Biotechnology (Dallas, TX, USA). Anti-IR antibody was purchased pre-
764 conjugated to Alexa Fluor 647 (Anti-INSR catalog # sc-57342 AF647; RRID:AB_784102); validated
765 by Wu and associates (Wu et al., 2019). Anti-IR antibody was generated against the C-terminus of
766 the beta subunit of human insulin receptor protein. FSU120, a rabbit polyclonal antiserum, was
767 generated against the 46-amino acid sequence 478-
768 MVIEEGGMNHSAFPQTPFKTGNSTATCTTNNNPNDCVNIKKIFTDV-523, representing the
769 unique coding region of the Kv1.3 channel between transmembrane domain 6 and the carboxy
770 terminal (Fadool *et al*., 2000). The purified peptide was produced by Genmed Synthesis (San
771 Francisco, CA, USA), the antiserum was produced and then affinity purified by Cocalico Biologicals
772 (Reamstown, PA, USA). We have validated this epitope in several previous studies (Fadool et al.,
773 2000, 2004; Colley et al., 2007; Marks and Fadool, 2007; Biju et al., 2008; Marks et al., 2009) and
774 this latest regeneration of the antisera, specifically (Velez et al., 2016; Kolling et al., 2022). Alexa
775 Fluor 546 (Invitrogen, catalog #A-11035; RRID:AB_2534077) was used to label the FSU120
776 antibody for imaging.

777

778 **Animals**

779 All mice were housed at the FSU vivarium on a standard 12 h/12 h light/dark cycle and in
780 accordance with institutional requirements for animal care. Mice were individually housed in
781 conventional-style rodent cages containing separate food and water that could be obtained *ad*
782 *libitum*. Mice were maintained on chow that was comprised of 13.5% kcal fat, 59.1% kcal
783 carbohydrate, and 28.05% kcal protein (Catalog #5001, Purina Company, St. Louis, MO,
784 USA).

785

786 B6:CBA-Tg(Tbx21-cre)1Dlc/J mice with cre recombinase expression limited to mitral and
787 tufted cells (catalog #024507, Jackson Labs, Bar Harbor, ME, USA;
788 RRID:IMSR_JAX:024507) were crossed with B6J.129(B6N)-Gt(ROSA)26Sor$^{tm1(CAG\text{-}cas9^{\wedge},\text{-}}$
789 $^{EGFP)Fezh}$/J mice (catalog #026175, Jackson Labs; RRID:IMSR_JAX:026175) to generate
790 progeny mice with bicistronic spCas9/EGFP expression limited to the mitral and tufted cells.

791 The EGFP signal, along with anticipated physiological parameters, was used to identify mitral
792 vs. tufted cells (Chen and Shepherd, 1997; Marks et al., 2009). A total of 78 Tbx21-cre x
793 Cas9/EGFP male and female mice were used in our experiments for electrophysiology and
794 RNAscope (referred to as simply 'GFP mice' throughout) and ranged from 19 to 28 postnatal
795 days (PD) in age. For Tbx21-cre x Cas9/EGFP mice that were used for
796 immunocytochemistry, mice were virally infected with an adenovirus carrying a sgRNA
797 [GCT GCC GCC AGA CAT GAC CG] that targeted a protospacer adjacent motif (PAM
798 recognition) target site that had close proximity to the 'start' codon of Kv1.3 to achieve
799 CRISPR editing of the channel selectively from mitral and tufted cells. sgRNA was packaged
800 into AAV9 viral particles (~3E+12 VG/ml) using a U6 promotor design (AAV9-hSyn-
801 mCherry-U6-sgRNA virus particle; SignaGen Laboratories). Retroorbital injection of the
802 sgRNA virus was performed on neonatal Tbx21-Cre x Cas9/EGFP mice at age PD5 as
803 previously described (Kolling et al., 2022). Immunocytochemistry experiments were
804 performed in mice that were subsequently raised to adult (greater than 6 month).
805
806 Kv1.3-/- mice were crossed with Thy1-YFP mice to generate progeny mice with
807 fluorescently-labeled OB neurons. Kv1.3-/- mice (RRID:IMSR_JAX:027392) were produced
808 previously by excision of the N-terminal one-third of the *Kv1.3* gene (Xu et al., 2003; Koni et
809 al., 2003) and were a generous gift from Drs. Leonard Kaczmarek and Richard Flavel (Yale
810 University, New Haven, CT, USA). Thy1-YFP mice (RRID:IMSR_JAX:014130) were a gift
811 from Dr. Gouping Feng (MIT Broad Institute, Boston, MA, USA) (Feng et al., 2000). A total
812 of 5 Kv1.3-/- x YFP male and female progeny mice were used for electrophysiology (referred
813 to as simply 'Kv1.3-/- mice' throughout) and ranged from PD19-28 in age. Homozygous
814 Kv1.3-/- mice (not crossed with Thy1-YFP) were also used for immunocytochemistry
815 experiments and compared with wildtype C57BL6/J lines (RRID:IMSR_JAX:000664) to
816 examine specificity of the Kv1.3 channel plus IR kinase labeling.
817

818 **Olfactory bulb slice recordings**

819 OB slices for electrophysiological recordings were acquired from GFP or Kv1.3-/- mice as
820 described previously (Fadool et al., 2011; Mast and Fadool, 2012; Huang et al., 2017;
821 Thiebaud et al., 2019; Kolling et al., 2022). Briefly, mice were anesthetized by inhalation of

822 isoflurane, quickly decapitated, and the OBs were rapidly exposed by removing the dorsal and
823 lateral portions of the skull (Nickell et al., 1996). The OBs (while still attached to the
824 forebrain) were quickly removed, glued to a sectioning block with Superglue (Lowe's Home
825 Improvement, Tallahassee, FL, USA) and submerged in oxygenated (95% O_2/5%CO_2), ice-
826 cold, sucrose-modified artificial cerebral spinal fluid (aCSF) to prepare the tissue for
827 sectioning. Coronal sections (300 μm) were cut in oxygenated, ice-cold, sucrose-modified
828 aCSF using a Series 1000 Vibratome (Leica, Wetzlar, Germany; RRID:SCR_016495). The
829 OB sections were allowed to recover in an interface chamber (Krimer and Goldman-Rakic,
830 1997) with oxygenated, sucrose-modified aCSF at 33° C for 15 min and then were maintained
831 at room temperature (rt) in oxygenated normal aCSF until needed (Fadool *et al*., 2011). OB
832 slices were recorded in a continuously-perfused (Ismatec; 1-2 ml/min), submerged-slice
833 recording chamber (RC-26, Warner Instruments, Hamden, CT, USA) with aCSF at rt.
834
835 OB slices were visualized at 10x and 40x using an Axioskop 2FS Plus Microscope (Carl Zeiss
836 Microimaging, Thornwood, NY, USA) equipped with fluorescent excitation and infrared
837 detection capabilities (CCD100; Dage-MTI, Michigan City, IN, USA). Electrodes were
838 fabricated from borosilicate glass (#1405002; Hilgenberg GmbH, Malsfeld, Germany) to a
839 diameter of ~2 μm to yield pipette resistances ranging from 4 to 8 MΩ. Positive pressure was
840 retained when navigating through the OB laminae until a high resistance seal (1.5–10 GΩ)
841 was obtained on a positionally-identified MC or sTC in the slice (Fadool et al., 2011). The
842 morphology and biophysical properties of the neurons were used to distinguish MCs and sTCs
843 (Nickell et al., 1996; Schoppa and Westbrook, 2001; Fadool et al., 2004; Fadool and Kolling,
844 2020). MCs were selected only if > 50% of their cell body resided within the MCL. sTCs
845 were selected only if their cell body resided in the outer one-third of the EPL, and were not
846 selected if their cell body partially resided within the GLM. In addition, GFP mice provided
847 fluorescent markers that served as secondary confirmation of cell identity, and were readily
848 distinguishable. The cell-attached configuration was established by applying gentle suction to
849 the lumen of the pipette while monitoring resistance. Whole-cell access was obtained by
850 applying a 100 ms, 1 mV pulse across the membrane while applying sharp suction to the
851 lumen of the pipette. Membrane voltage and current properties were generated using
852 pCLAMP, version 9 or 10, in conjunction with a Multiclamp 700B amplifier (Axon

853 Instruments; RRID:SCR_011323/Molecular Devices; RRID:SCR_018455). The analog signal
854 was filtered at 3 kHz and minimally digitally sampled every 100 μs with a Digidata 1440A
855 digitizer (Axon Instruments, Molecular Devices; RRID:SCR_021038). The pipette
856 capacitance was electrically compensated through the capacitance neutralization circuit of the
857 Multiclamp 700B amplifier. Resting membrane potentials were corrected for a calculated -7
858 mV junction potential offset. Membrane capacitance was acquired from the membrane test
859 function of Clampex 10.7 (Axon Instruments, RRID:SCR_011323). Input resistance was
860 calculated using Ohm's law by injecting a -50 pA current and measuring the induced voltage
861 deflection. For clarity across disciplines, this report uses the electrophysiological terminology
862 that is used by the pCLAMP software suite. Where applicable, other common names are
863 included in parentheses.
864
865 After establishing a whole-cell configuration, cells were first sampled for adequate resting
866 potential (less than -50 mV), proper access resistance (less than 40 MΩ), and adequate input
867 resistance (greater than 150 MΩ) prior to initiating either a series of current- or voltage-clamp
868 recordings. For current-clamp recordings, cells were held at -60 mV (near rest; V_h) between
869 pulses to compare data across cells. Peri-threshold current levels were determined by
870 incrementally injecting a family of current pulses of 1000 millisecond (ms) duration (P_d).
871 Current was injected every 30 seconds (s) and was stepped in 25 pA increments from -50 pA
872 to 175 pA to obtain action potential (AP) characteristics and current-dependence data.
873 Following the determination of spike threshold, cells were stimulated with 10 super-threshold
874 sweeps using a P_d of 5000 ms (typically ranging from 15 to 150 pA) every 30 s (T_s) to acquire
875 spike frequency and latency data. Current-clamp data were acquired in the presence of
876 synaptic blockers and voltage-clamp data were acquired in the presence of 20 μM TTX to
877 eliminate unwanted AP spiking (see Solutions).
878
879 AP characteristics, latency to first spike, spike event frequency, interspike interval, intratrain
880 interval, and spike train length were measured using Clampfit software as described
881 previously (Balu et al., 2004; Fadool et al., 2011; Mast and Fadool, 2012). A train was defined
882 as three or more consecutive spikes within a period of 100 ms or less, as established by Balu
883 et al. (Balu et al., 2004). M/TC firing is intrinsically intermittent and is characterized by

884 variable train characteristics. As such, classical means of computing spike timing variability,
885 such as peri-stimulus time histograms, were less suitable for the behavior of these neurons.
886 Therefore, alternative means of spike analysis were applied as described previously (Balu et
887 al., 2004; Fadool et al., 2011; Thiebaud et al., 2016; Kolling et al., 2022). For voltage-clamp
888 recordings, cells were held at -80 mV (V_h), then stepped from -100 mV to +40 mV (V_c) in
889 +20 mV increments for a duration of 400 ms (P_d) with a stimulation interval (T_s) of 45 s.
890
891 **Tissue Preparation and Immunocytochemistry**
892
893 Mice were deeply anesthetized and then terminated by cardiac perfusion using 4% PFA as
894 previously described (Thiebaud et al., 2014). The mice were decapitated, and brains carefully
895 removed from the skulls to flash freeze the brain in protective medium (Biju et al., 2008).
896 More detailed immunocytochemistry procedures can be found in our previous works (Biju et
897 al., 2008; Thiebaud et al., 2014), and current parameters for this project were as follows.
898 Coronal sections at 25-µm thickness (Model 1850UV, Leica Biosystems) were prepared for
899 slide-mounting. Labeling control consisted of blocking and incubation in buffer without
900 antibodies. No-primary (omission of FSU120 primary antisera) and singly-labeled controls
901 were performed to determine the specificity of the anti-rabbit secondary antibody with pre-
902 conjugated antibodies. Sections were blocked with 3% goat sera and incubation of primary
903 antisera took place overnight at 4ºC (1:1000 anti-INSR, 1:1000 FSU120) with secondary
904 antisera (1:500 Alexa Fluor 486) incubation following the next day for 2 h at room
905 temperature. Slides were cover-slipped using Vectashield mounting media containing DAPI
906 (H1200-10, Vector Laboratories, Newark, CA) before imaging. Imaging was performed on a
907 Yokogawa Series Nikon Spinning Disk Confocal Microscope (Nikon Instruments, Inc.,
908 Melville NY, USA; Model CSUW1, RRID:SCR_021741) using a 20X lens, and appropriate
909 laser lines for each reporter (475 nm, 551 nm, 642 nm). Post-hoc analyses were performed
910 using Photoshop CS4 (Adobe, San Jose, CA, USA; RRID:SCR_014199). The minimum and
911 maximum thresholds for each color channel were adjusted uniformly for all images before
912 using the "difference" feature to align multidimensional images in Photoshop. This method
913 allowed for transient removal of specific channels in order to more clearly determine co-
914 localization of reporters.

915

916 **RNA scope and quantification**

917 Five male and five female GFP mice (10 mice total) were anesthetized with ketamine/xylazine
918 and fixed via transcardial perfusion of PBS followed by 4% PFA. Brains were cryoprotected
919 in 30% sucrose before being embedded in OCT and flash frozen. Mouse brains were
920 cryosectioned coronally at 16 µm, and sections were collected 1:10. Sections were mounted
921 on histobond glass slides, and RNAscope was performed according to the ACDbio
922 manufacturer's protocol using commercially available probes for *GFP, Kv1.3* and *Insr*. The
923 sequence of the mouse *GFP* transgene was used to verify the selection of GFP RNAscope
924 probe. Images were acquired using an Olympus VS200 slidescanner at 20X, and analysis was
925 performed using QuPath software (v 0.5). The 'cell detection' function was first used to
926 identify Tbx21+ cells, then object classifiers were created for *Kv1.3* and *Insr* using a threshold
927 for mean fluorescent intensity within each cell. Validation of this workflow was performed
928 manually, once per neurolaminar layer (MCL, EPL, and GLM).

929

930 **Experimental design and statistical analyses**

931 Before performing any statistical comparisons, data were first analyzed with the Dixon's Q
932 test to identify any outliers. Data were then checked for normal distribution and homogeneity
933 of variance using the Fmax test. Analysis of data collected did not identify any outliers.
934 Where collected data violated homogeneity of variance (failed the Fmax test), the selection of
935 applied statistics was changed to the nonparametric equivalent. Paired comparisons (innate
936 properties, action potential kinetics, bursting metrics) were analyzed using Student's *t* test or
937 Mann-Whitney U at the 95% confidence level ($\alpha < 0.05$). There were no sex-specific
938 differences in the measured parameters, so measurements from both sexes were combined. IV
939 plots, frequency and interspike interval (ISI) were analyzed using a mixed two-way RM
940 ANOVA with current and voltage as factors (IV) or current and cell type as factors (frequency
941 and ISI); at the 95% confidence level ($\alpha < 0.05$). Modulation of voltage-activated current
942 between cell types was analyzed using a mixed three-way RM ANOVA with voltage, cell
943 type, and drug as factors; at the 95% confidence level ($\alpha < 0.05$). Insulin modulation data
944 were analyzed using within-cell comparisons by applying a paired *t* test at the 95% confidence
945 level ($\alpha < 0.05$). Categorical AP spike train type analysis was performed using a Chi-Square

test, where the expected proportion of sTCs eliciting spike trains was set as the observed proportion of MCs eliciting spike trains; 95% confidence level ($\alpha < 0.05$). For the two-way RM ANOVA tests, the Sidak method for multiple comparison testing was used as the post-hoc analysis to make mean-wise comparisons between cell types or between drug treatments. All reported values in the text represent the mean ± SD. Figures largely report individual data points using violin graphs and represent number of cells as noted in the figure legends. Sample sizes for the line graphs are reported in the figure legends. Where means are reported in the figures, the error is reported as the SEM. Individual *p* values are reported for each experiment within the corresponding graph with the individual F statistic described in the results section. Statistical tests were performed using GraphPad Prism 9 (GraphPad Software) while the graphs and figures were produced using a combination of Origin v8 (OriginLab Corporation; RRID:SCR_014212), Adobe Photoshop CS4 (Adobe; RRID:SCR_014199), and GraphPad Prism 9 (GraphPad Software; RRID:SCR_002798).

All electrophysiological data were analyzed using pClamp, version 10 (Clampfit 10.7; Molecular Devices; RRID:SCR_011323) and Igor Pro, version 6.12A (WaveMetrics Inc.; RRID:SCR_000325) with the plug-in NeuroMatic, version 2 (written by Jason Rothman; http://www.neuromatic.thinkrandom.com; RRID:SCR_004186). Exact *p* values, statistical tests, and parameters are given in the results text/figures for each data set. Specific variables required for independent replication (sample size, number of animals, etc.) and full statistical reporting can be found in the methods and results text/figures for each respective experiment and the supplemental statistical table (Supplemental Table 1).

ACKNOWLEDGEMENTS

We would like to thank Carley Huffstetler, Alexis Cox, Tyla Dolezel, and Franklin Pacheco for routine technical assistance and in maintaining mouse colonies. We would like to thank Jaime White-James for the oversight of our animal husbandry and routine mouse care needs.

AI USE

The authors declare that no AI tools were used for this manuscript including scientific writing, generation of code, production of images, or in the collection or analyses of data.

COMPETING INTERESTS

The authors have no interests to declare, scientific or financial.

AUTHOR CONTRIBUTIONS

All authors critically evaluated the work for important intellectual content. All authors acquired, analyzed, or interpreted data in the study. As such, we confirm that all approved the final version of the manuscript; agreed to be accountable for all aspects of the work in ensuring that questions related to the accuracy or integrity of any part of the work are appropriately investigated and resolved; and all persons designated as authors qualify for authorship, and all who qualify for authorship are listed. In using the CRediT (Contributor Roles Taxonomy) guidelines, L.K. and D.F. were responsible for project conceptualization, data curation, formal analysis, funding acquisition, methodology, validation, visualization, and writing the original draft, reviewing, and editing. L.K. was responsible for electrophysiological recordings. S.M. was responsible for methodology and immunocytochemistry experiments. C.M. and D.F. were responsible for project administration and supervision. L.K., C.M. and D.F. were responsible for the provision of resources.

FUNDING

This work was supported by the United States Department of Agriculture NIFA Predoctoral Fellowship 2019-07151, an endowment from the Robinson Family and the Tallahassee Memorial Hospital, a grant from the Higher Education Emergency Relief Fund (HEERF II), a

grant from the National Institute on Aging (NIA) at NIH as F32AG084196, and a grant from the National Institute of Diabetes, and Digestive and Kidney Diseases (NIDDK) at NIH as R01DK133464.

DATA AVAILABILITY

All data referenced in this report are summarized in the primary figures contained in the publication. All summarized electrophysiological recordings data are stored in the Fadool Laboratory and are available upon request.

REFERENCES

Aimé P, Hegoburu C, Jaillard T, Degletagne C, Garcia S, Messaoudi B, Thevenet M, Lorsignol A, Duchamp C, Mouly AM and Julliard AK (2012). A physiological increase of insulin in the olfactory bulb decreases detection of a learned aversive odor and abolishes food odor-induced sniffing behavior in rats. *PLoS One* **7,** e51227–e51227.

Antal M, Eyre M, Finklea B and Nusser Z (2006). External tufted cells in the main olfactory bulb form two distinct subpopulations. *Eur J Neurosci* **24(4),** 1124-1136.

Arnold SE, Arvanitakis Z, Macauley-Rambach SL, Koenig AM, Wang H-Y, Ahima RS, Craft S, Gandy S, Buettner C, Stoeckel LE, Holtzman DM and Nathan DM (2018). Brain insulin resistance in type 2 diabetes and Alzheimer disease: Concepts and conundrums. *Nature Rev Neurol* **14,** 168–181.

Balu R, Larimer P and Strowbridge BW (2004). Phasic stimuli evoke precisely timed spikes in intermittently discharging mitral cells. *J Neurophysiol* **92,** 743–753.

Banks WA, Kastin AJ and Pan W (1999). Uptake and degradation of blood-borne insulin by the olfactory bulb. *Peptides* **20,** 373–378.

Bartok A, Toth A, Somodi S, Szanto TG, Hajdu P, Panyi G and Varga Z (2014). Margatoxin is a non-selective inhibitor of human Kv1.3 K+ channels. *Toxicon* **87,** 6–16.

Baskin DG, Porte Jr. D, Guest K and Dorsa DM (1983). Regional concentrations of insulin in the rat brain. *Endocrinol* **112,** 898–903.

Biju KC, Marks DR, Mast TG and Fadool DA (2008). Deletion of voltage-gated channel affects glomerular refinement and odorant receptor expression in the mouse olfactory system. *J Comp Neurol* **506,** 161–179.

1032 Bowlby MR, Fadool DA, Holmes TC and Levitan IB (1997). Modulation of the Kv1.3 potassium
1033 channel by receptor tyrosine kinases. *J Gen Physiol* **110,** 601–610.

1034 Burry RW (2011). Controls for immunocytochemistry: An update. *J Histochem Cytochem* **59,** 6.

1035 Burton SD and Urban NN (2014). Greater excitability and firing irregularity of tufted cells underlies
1036 distinct afferent-evoked activity of olfactory bulb mitral and tufted cells. *J Physiol* **592,** 2097.

1037 Chen F, He A, Tang Q, Li S, Liu X, Yin Z, Yao Q, Yu Y and Li A (2024). Cholecystokinin-
1038 expressing superficial tufted cells modulate odour representation in the olfactory bulb and
1039 olfactory behaviours. *J Phyiol* **602(14),** 3519-3543.

1040 Chen R and Chung SH (2014). Binding modes of two scorpion toxins to the voltage-gated potassium
1041 channel kv1.3 revealed from molecular dynamics. *Toxins (Basel)* **6,** 2149–2161.

1042 Coecke S, Balls M, Bowe G, Davis J, Gstraunthaler G, Hartung T, Hay R, Merten OW, Price A,
1043 Schechtman L, Stacey G and Stokes W (2005). Guidance on good cell culture practice. A report
1044 of the second ECVAM task force on good cell culture practice. *Altern Lab Anim* **33,** 261–287.

1045 Colley B, Tucker K and Fadool DA (2004). Comparison of modulation of Kv1.3 channel by two
1046 receptor tyrosine kinases in olfactory bulb neurons of rodents. *Recept Channels* **10,** 25–36.

1047 Colley BS, Biju KC, Visegrady A, Campbell S and Fadool DA (2007). Neurotrophin B receptor
1048 kinase increases Kv subfamily member 1.3 (Kv1.3) ion channel half-life and surface expression.
1049 *Neuroscience* **144,** 531–546.

1050 Colley BS, Cavallin MA, Biju K, Marks DR and Fadool DA (2009). Brain-derived neurotrophic
1051 factor modulation of Kv1.3 channel is disregulated by adaptor proteins Grb10 and nShc. *BMC*
1052 *Neurosci* **10,** 8.

1053 Cook KK and Fadool DA (2002). Two adaptor proteins differentially modulate the phosphorylation
1054 and biophysics of Kv1.3 ion channel by Src kinase. *J Biol Chem* **277,** 13268–13280.

1055 Das P, Parsons AD, Scarborough J, Hoffman J, Wilson J, Thompson RN, Overton JM and Fadool
1056 DA (2005). Electrophysiological and behavioral phenotype of insulin receptor defective mice.
1057 *Physiol Behav* **86,** 287–296.

1058 De Saint Jan D, Hirnet D, Westbrook GL and Charpak S (2009). External tufted cells drive the
1059 output of olfactory bulb glomeruli. *J Neurosci* **29(7),** 2043-2052.

1060 Fadool DA, Holmes TC, Berman K, Dagan D and Levitan IB (1997). Tyrosine phosphorylation
1061 modulates current amplitude and kinetics of a neuronal voltage-gated potassium channel. *J*
1062 *Neurophysiol* **78,** 1563–1573.

1063 Fadool DA and Kolling LJ (2020). Role of olfaction for eating behavior. In *The Senses: A*
1064 *Comprehensive Reference*, Second Edi., ed. Fritzsch B and Meyerhof W, pp. 675–716. Elsevier.

1065 Fadool DA and Levitan IB (1998). Modulation of olfactory bulb neuron potassium current by
1066 tyrosine phosphorylation. *J Neurosci* **18,** 6126–6137.

1067 Fadool DA, Tucker K and Pedarzani P (2011). Mitral cells of the olfactory bulb perform metabolic
1068 sensing and are disrupted by obesity at the level of the Kv1.3 ion channel. *PLoS One* **6,** e24921.

1069 Fadool DA, Tucker K, Perkins R, Fasciani G, Thompson RN, Parsons AD, Overton JM, Koni PA,
1070 Flavell RA and Kaczmarek LK (2004). Kv1.3 channel gene-targeted deletion produces "Super-
1071 Smeller Mice" with altered glomeruli, interacting scaffolding proteins, and biophysics. *Neuron*
1072 **41,** 389–404.

1073 Fadool DA, Tucker K, Phillips JJ and Simmen JA (2000). Brain insulin receptor causes activity-
1074 dependent current suppression in the olfactory bulb through multiple phosphorylation of Kv1.3.
1075 *J Neurophysiol* **83,** 2332–2348.

1076 Femminella GD *et al*. (2021). Does insulin resistance influence neurodegeneration in non-diabetic
1077 Alzheimer's subjects? *Alzheimer's Res & Ther* **13,** 1–11.

1078 Feng G, Mellor RH, Bernstein M, Keller-Peck C, Nguyen QT, Wallace M, Nerbonne JM, Lichtman
1079 JW and Sanes JR (2000). Imaging neuronal subsets in transgenic mice expressing multiple
1080 spectral variants of GFP. *Neuron* **28,** 41–51.

1081 Ferreira LSS, Fernandes CS, Vieira MNN and De Felice FG (2018). Insulin resistance in Alzheimer's
1082 disease. *Front Neurosci* **12,** 830.

1083 Gadiwalla, S, Guillaume C, Huang L, White SJB, Basha N, Petersen PH and Galliano E (2025) *Ex*
1084 *vivo* functional characterization of mouse olfactory bulb projection neurons reveals a
1085 heterogeneous continuum. *eNeuro* 12(3), ENEURO.0407-24.2025.

1086 Garcia ML, Hanner M, Knaus HG, Koch R, Schmalhofer W, Slaughter RS and Kaczorowski GJ
1087 (1997). Pharmacology of potassium channels. *Adv Pharmacol* **39,** 425–471.

1088 Garcia-Calvo M, Leonard RJ, Novick J, Stevens SP, Schmalhofer W, Kaczorowski GJ and Garcia
1089 ML (1993). Purification, characterization, and biosynthesis of margatoxin, a component of
1090 Centruroides margaritatus venom that selectively inhibits voltage-dependent potassium
1091 channels. *J Biol Chem* **268,** 18866–18874.

1092 Gire DH, Franks KM, Zak JD, Tanaka KF, Whitesell JD, Mulligan AA, Hen R and Schoppa NE
1093 (2012). Mitral cells in the olfactory bulb are mainly excited through a multistep signaling path. *J*
1094 *Neurosci* **32,** 2964–2975.

1095 Grundy D (2015). Principles and standards for reporting animal experiments in The Journal of
1096 Physiology and Experimental Physiology. *J Physiol* **593,** 2547–2549.

1097 Gupta G, Azam M and Baquer NZ (1992). Modulation of rat brain insulin receptor kinase activity in
1098 diabetes. *Neurochem Int* **20,** 487–492.

1099 Hayar A, Karnup S, Shipley MT and Ennis M (2004a). Olfactory bulb glomeruli: External tufted
1100 cells intrinsically burst at theta frequency and are entrained by patterned olfactory input. *J*
1101 *Neurosci* **24(5),** 1190-1199.

1102 Hayar A, Karnup S, Ennis M and Shipley MT (2004b). External tufted cells: A major excitatory
1103 element that coordinates glomerular activity. *J Neurosci* **24,** 6676–6685.

1104 Hayar A, Shipley MT and Ennis M (2005) Olfactory bulb external tufted cells are synchronized by
1105 multiple intraglomerular mechanisms. *J Neurosci* **25(36),** 8197-8208.

1106 Hill JM, Lesniak MA, Pert CB and Roth J (1986). Autoradiographic localization of insulin receptors
1107 in rat brain: Prominence in olfactory and limbic areas. *NeuroSci* **17,** 1127–1136.

1108 Holmes TC, Fadool DA and Levitan IB (1996). Tyrosine phosphorylation of the Kv1.3 potassium
1109 channel. *J Neurosci* **16,** 1581–1590.

1110 Hong S, Han K and Park C-Y (2021). The insulin resistance by triglyceride glucose index and risk for
1111 dementia: population-based study. *Alzheimer's Res & Ther* **13,** 1–10.

1112 Huang Z, Thiebaud N and Fadool DA (2017). Differential serotonergic modulation across the main
1113 and accessory olfactory bulbs. *J Physiol* **595,** 3515–3533.

1114 Igarashi KM, Ieki N, An M, Yamaguchi Y, Nagayama S, Kobayakawa K, Kobayakawa R, Tanifuji
1115 M, Sakano H, Chen WR and Mori K (2012). Parallel mitral and tufted cell pathways route
1116 distinct odor information to different targets in the olfactory cortex. *J Neurosci* **32,** 7970–7985.

1117 Jan DD Saint and Westbrook GL (2007). Disynaptic amplification of metabotropic Glutamate
1118 Receptor 1 responses in the olfactory bulb. *J Neurosci* **27,** 132–140.

1119 Jones S, Zylberberg J and Schoppa N (2020). Cellular and synaptic mechanisms that differentiate
1120 mitral cells and superficial tufted cells into parallel output channels in the olfactory bulb. *Front*
1121 *Cell Neurosci* **14,** 443.

1122 Kolling LJ, Tatti R, Lowry T, Loeven AM, Fadool JM and Fadool DA (2022). Modulating the
1123 excitability of olfactory output neurons affects whole-body metabolism. *J Neurosci* **42,** 5966–
1124 5990.

1125 Koni PA, Khanna R, Chang MC, Tang MD, Kaczmarek LK, Schlichter LC and Flavell RA (2003).
1126 Compensatory anion currents in Kv1.3 channel-deficient thymocytes. *J Biol Chem* **278,** 39443–
1127 39451.

1128 Krimer LS and Goldman-Rakic PS (1997). An interface holding chamber for anatomical and
1129 physiological studies of living brain slices. *J Neurosci Meth* **75,** 55–58.

1130 Kuczewski N, Fourcaud-Trocmé N, Savigner A, Thevenet M, Aimé P, Garcia S, Duchamp-Viret P
1131 and Palouzier-Paulignan B (2014). Insulin modulates network activity in olfactory bulb slices:
1132 impact on odour processing. *J Physiol* **592,** 2751–2769.

1133 Kues WA and Wunder F (1992). Heterogeneous expression patterns of mammalian potassium
1134 channel genes in developing and adult rat brain. *Eur J Neurosci* **4,** 1296–1308.

1135 Kuljiš RO and Salković-Petrišić M (2011). Dementia, diabetes, Alzheimer's disease, and insulin
1136 resistance in the brain: progress, dilemmas, new opportunities, and a hypothesis to tackle
1137 intersecting epidemics. *J Alzheimer's Dis* **25,** 29–41.

1138 Liu A, Savya S and Urban NN (2016). Early odorant exposure increases the number of mitral and
1139 tufted cells associated with a single glomerulus. *J Neurosci* **36,** 11646–11653.

1140 Liu S and Shipley MT (2008). Multiple conductances cooperatively regulate spontaneous bursting in
1141 mouse olfactory bulb external tufted cells. *J Neurosci* **28,** 1625.

1142 Lu S, Das P, Fadool DA and Kaczmarek LK (2010). The slack sodium-activated potassium channel
1143 provides a major outward current in olfactory neurons of Kv1.3-/- super-smeller mice. *J*
1144 *Neurophysiol* **103,** 3311–3319.

1145 Ma J and Lowe G. (2007). Correlated firing in tufted cells of mouse olfactory bulb. *Neurosci*
1146 **169(4),** 1715-1738.

1147 Marks DR and Fadool DA (2007). Post-synaptic density perturbs insulin-induced Kv1.3 channel
1148 modulation via a clustering mechanism involving the SH3 domain. *J Neurochem* **103,** 1608–
1149 1627.

1150 Marks DR, Tucker K, Cavallin MA, Mast TG and Fadool DA (2009). Awake intranasal insulin
1151 delivery modifies protein complexes and alters memory, anxiety, and olfactory behaviors.28. *J*
1152 *Neurosci* **29,** 6734–6751.

1153 Marks JL, Porte D Jr, Stahl WL, and Baskin DG (1990). Localization of insulin receptor mRNA in
1154 rat brain by in situ hybridization. *Endocrinology* **127(6),** 3234-3236.

1155 Mast TG and Fadool DA (2012). Mature and precursor brain-derived neurotrophic factor have
1156 individual roles in the mouse olfactory bulb. *PLoS ONE* **7,** e31978–e31978.

1157 Mitsui S, Igarashi KM, Mori K, and Yoshihara Y (2011). Genetic visualization of the secondary
1158 olfactory pathway in Tbx21 transgenic mice. *Neural Syst Circuits* **1(1),** 5.

1159 Mori K (1987). Membrane and synaptic properties of identified neurons in the olfactory bulb. *Prog*
1160 *Neurobiol* **29,** 275–300.

1161 Mori K and Sakano H (2022). Processing of odor information during the respiratory cycle in mice.
1162 *Front Neural Circ* **16,** 861800.

1163 Myers Jr. MG and White MF (1993). The new elements of insulin signaling. Insulin receptor
1164 substrate-1 and proteins with SH2 domains. *Diabetes* **42,** 643–650.

1165 Nagayama S, Enerva A, Fletcher ML, Masurkar A V, Igarashi KM, Mori K and Chen WR (2010).
1166 Differential axonal projection of mitral and tufted cells in the mouse main olfactory system.
1167 *Front Neural Circ* **4,** 120

1168 Nagayama S, Homma R and Imamura F (2014). Neuronal organization of olfactory bulb circuits.
1169 *Front Neural Circuits* **8,** 98.

1170 Najac M, Jan D de Saint, Reguero L, Grandes P and Charpak S (2011). Monosynaptic and
1171 polysynaptic feed-forward inputs to mitral cells from olfactory sensory neurons. *J Neurosci* **31,**
1172 8722–8729.

1173 Nickell WT, Shipley MT and Behbehani MM (1996). Orthodromic synaptic activation of rat
1174 olfactory bulb mitral cells in isolated slices. *Brain Res Bull* **39,** 57–62.

1175 Nikouee A, Khabiri M, Grissmer S and Ettrich R (2012). Charybdotoxin and margatoxin acting on
1176 the human voltage-gated potassium channel h Kv1.3 and its H399N mutant: An experimental
1177 and computational comparison. *J Phys Chem B* **116,** 5132–5140.

1178 Palouzier-Paulignan B, Lacroix MC, Aime P, Baly C, Caillol M, Congar P, Julliard AK, Tucker K
1179 and Fadool DA (2012). Olfaction under metabolic influences. *Chem Senses* **37,** 769–797.

1180 Pinching AJ and Powell TPS (1971a). The neuropil of the periglomerular region of the olfactory
1181 bulb. *J Cell Sci* **9(2),** 379-409.

1182 Pinching AJ and Powell TPS (1971b). The neuron types of the glomerular layer of the olfactory bulb.
1183 *J Cell Sci* **9(2),** 305–345.

1184 Price JL and Powell TP (1970). The mitral and short axon cells of the olfactory bulb. *J Cell Sci* **7,**
1185 631–651.

1186 Salameh S, Nouel D, Flores C and Hoops D (2017). An optimized immunohistochemistry protocol
1187 for detecting the guidance cue Netrin-1 in neural tissue. *MethodsX* **5,** 1–7.

1188 Saper CB (2009). A guide to the perplexed on the specificity of antibodies. *J Histochem Cytochem*
1189 **57,** 1.

1190 Schoppa NE and Westbrook GL (2001). Glomerulus-specific synchronization of mitral cells in the
1191 olfactory bulb. *Neuron* **31,** 639–651.

1192 Schwartz MW, Figlewicz DP, Baskin DG, Woods SC and Porte Jr. D (1992). Insulin in the brain: a
1193 hormonal regulator of energy balance. *Endocr Rev* **13,** 387–414.

1194 Shepherd GM (2004). *The synaptic organization of the brain*, 5th ed. Shepherd GM. Oxford
1195 University Press.

1196 Spencer VA, Kumar S, Paszkiet B, Fein J and Zmuda JF (2014). Cell culture media for fluorescence
1197 imaging. *Genet Eng Biotechnol News **34,** 10.*

1198 Thiebaud N, Gribble F, Reimann F, Trapp S and Fadool DA (2019). A unique olfactory bulb
1199 microcircuit driven by neurons expressing the precursor to glucagon-like peptide 1. *Scientific*
1200 *Rep* **9,** 15542.

1201 Thiebaud N, Johnson MC, Butler JL, Bell GA, Ferguson KL, Fadool AR, Fadool JC, Gale AM, Gale
1202 DS and Fadool DA (2014). Hyperlipidemic diet causes loss of olfactory sensory neurons,
1203 reduces olfactory discrimination, and disrupts odor-reversal learning. *J Neurosci* **34,** 6970–6984.

1204 Thiebaud N, Llewellyn-Smith IJ, Gribble F, Reimann F, Trapp S and Fadool DA (2016). The incretin
1205 hormone glucagon-like peptide 1 increases mitral cell excitability by decreasing conductance of
1206 a voltage-dependent potassium channel. *J Physiol* **594,** 2607–2628.

1207 Tucker K, Cavallin MA, Jean-Baptiste P, Biju KC, Overton JM, Pedarzani P and Fadool DA (2010).
1208 The Olfactory Bulb: A Metabolic Sensor of Brain Insulin and Glucose Concentrations via a
1209 Voltage-Gated Potassium Channel. *Results Probl Cell Differ* **52,** 147–157.

1210 Tucker K, Cho S, Thiebaud N, Henderson MX and Fadool DA (2013). Glucose sensitivity of mouse
1211 olfactory bulb neurons is conveyed by a voltage-gated potassium channel. *J Physiol* **591,** 2541–
1212 2561.

1213 Tucker K and Fadool DA (2002). Neurotrophin modulation of voltage-gated potassium channels in
1214 rat through TrkB receptors is time and sensory experience dependent. *J Physiol* **542,** 413–429.

1215 Vaaga CE and Westbrook GL (2016). Parallel processing of afferent olfactory sensory information. *J*
1216 *Physiol* **594,** 6715.

1217 Velez P, Schwartz AB, Iyer SR, Warrington A and Fadool DA (2016). Ubiquitin ligase Nedd4-2
1218 modulates Kv1.3 current amplitude and ion channel protein targeting155. *J Neurophysiol* **116,**
1219 671–685.

1220 White MF (1997). The insulin signalling system and the IRS proteins. *Diabetologia* **40 Suppl 2,** S2-
1221 17.

1222 Wickelgren I (1998). Tracking insulin to the mind. *Science (1979)* **280,** 517–519.

1223 Wu S, Zhang Y and De Luca F (2019). The effect of a high-calorie diet on bone growth is mediated
1224 by the insulin receptor. *Bone* 166–175.

1225 Xu J, Koni PA, Wang P, Li G, Kaczmarek L, Wu Y, Li Y, Flavell RA and Desir G V (2003). The
1226 voltage-gated potassium channel Kv1.3 regulates energy homeostasis and body weight. *Human*
1227 *Mol Gen* **12,** 551–559.

1228 Youngstrom IA and Strowbridge BW (2015). Respiratory modulation of spontaneous subthreshold
1229 synaptic activity in olfactory bulb granule cells recorded in awake, head-fixed mice. *J Neurosci*
1230 **35,** 8758.

1231 Zagotta WN and Aldrich RW (1990). Alterations in activation gating of single Shaker A-type
1232 potassium channels by the Sh5 mutation. *J Neurosci* **10,** 1799–1810.

1233 Zeppilli S, Ackels T, Attey R, Klimpert N, Ritola KD, Boeing S, Crombach A, Schaefer AT, and
1234 Fleischmann A (2021). Molecular characterization of projection neuron subtypes in the mouse
1235 olfactory bulb. *ELife* **10**, e65445.

1236 Zhou F-W, Hook C and Puche AC (2023). Frequency-dependent centrifugal modulation of the
1237 activity of different classes of mitral and tufted cells in olfactory bulb. *J Neurophysiol* **129,**
1238 1515–1533.

1239 Zhou Z, Xiong W, Zeng S, Xia A, Shepherd GM, Greer CA and Chen WR (2006). Dendritic
1240 excitability and calcium signaling in the mitral cell distal glomerular tuft. *Eur J Neurosci* **24(6),**
1241 1623-1632.

1242

1243

1244

1245

1246